STRUCTURAL BIOLOGY

Ratchet-like polypeptide translocation mechanism of the AAA+ disaggregase Hsp104

Stephanie N. Gates,[1,2]* Adam L. Yokom,[1,2]* JiaBei Lin,[3] Meredith E. Jackrel,[3] Alexandrea N. Rizo,[2] Nathan M. Kendsersky,[3,4] Courtney E. Buell,[3] Elizabeth A. Sweeny,[3] Korrie L. Mack,[3,5] Edward Chuang,[3,4] Mariana P. Torrente,[3,6] Min Su,[1] James Shorter,[3,4,5] Daniel R. Southworth[1,2]†

Hsp100 polypeptide translocases are conserved members of the AAA+ family (adenosine triphosphatases associated with diverse cellular activities) that maintain proteostasis by unfolding aberrant and toxic proteins for refolding or proteolytic degradation. The Hsp104 disaggregase from *Saccharomyces cerevisiae* solubilizes stress-induced amorphous aggregates and amyloids. The structural basis for substrate recognition and translocation is unknown. Using a model substrate (casein), we report cryo–electron microscopy structures at near-atomic resolution of Hsp104 in different translocation states. Substrate interactions are mediated by conserved, pore-loop tyrosines that contact an 80-angstrom-long unfolded polypeptide along the axial channel. Two protomers undergo a ratchet-like conformational change that advances pore loop–substrate interactions by two amino acids. These changes are coupled to activation of specific nucleotide hydrolysis sites and, when transmitted around the hexamer, reveal a processive rotary translocation mechanism and substrate-responsive flexibility during Hsp104-catalyzed disaggregation.

Hsp100 disaggregases are highly conserved stress responders that unfold and solubilize protein aggregates (*1*, *2*). They hexameric ring complexes, which couple adenosine triphosphate (ATP) hydrolysis to polypeptide translocation through a central channel (*1*, *2*). *Saccharomyces cerevisiae* Hsp104 is powered by two distinct AAA+ (ATPases associated with diverse cellular activities) domains per protomer and collaborates with the Hsp70 system to disaggregate and refold amorphous aggregates and amyloids such as Sup35 prions, thereby promoting stress tolerance and prion propagation (*2*).

Cooperative ATP hydrolysis by nucleotide-binding domains (NBD1 and NBD2) of Hsp104 requires conserved Walker A and B motifs, "sensor" residues, and an Arg finger from the adjacent protomer (*2*, *3*). The coiled-coil middle domain (MD) of Hsp104 mediates Hsp70 interactions and allosteric functions during hydrolysis and disaggregation (*4*–*6*). Conserved substrate-binding "pore loops" in the NBDs line the axial channel and contain essential Tyr residues that mechanically couple hydrolysis to translocation (*7*, *8*). A recently described structure of Hsp104 bound to the nonhydrolyzable ATP analog adenylyl-imidodiphosphate (AMP-PNP) identifies an "open," spiral conformation with a ~30-Å-wide channel and an unusual heteromeric NBD1-NBD2 interaction that forms a flexible seam (*9*). High-resolution structures of the active hexamer have remained elusive, and it is unknown how hydrolysis and conformational changes power disaggregation.

Here we establish how Hsp104 binds and mechanically translocates substrates. Using the slowly hydrolyzable ATP analog adenosine 5′-*O*-(3-thiotriphosphate) (ATP-γ-S) (*10*) and the substrate casein, we determined Hsp104 structures to ~4.0 Å by cryo–electron microscopy (cryo-EM). We identify pore loop–substrate contacts and a rotary translocation mechanism involving a ratchet-like change that advances interactions along the substrate polypeptide by two amino acids. NBD1-ATP hydrolysis and substrate binding trigger a massive open-to-closed conformational change in the hexamer, thereby coupling substrate engagement and release to processive disaggregation.

Substrate-bound architecture of Hsp104

To capture the substrate-bound state of Hsp104, binding was assessed with fluorescence polarization by using fluorescein isothiocyanate (FITC)–labeled casein, a model substrate that is actively translocated (*4*, *8*). High-affinity interactions (K_d ~ 20 nM) between Hsp104 and casein were identified in the presence of ATP-γ-S, but not ATP, AMP-PNP, or adenosine diphosphate (ADP) (Fig. 1A and fig. S1). Two-dimensional (2D) reference-free classification of purified Hsp104:casein–ATP-γ-S complexes revealed that the hexamer undergoes a large rearrangement compared to the AMP-PNP–bound open state (*9*) (Fig. 1B and fig. S2A). An initial 3D structure refined to ~3.9 Å resolution (fig. S2B and table S1). However, a two-protomer site was identified to be flexible (fig. S2C). Extensive 3D classification resolved these protomers and revealed two hexamer conformations: "closed" and "extended" (fig. S2D). Refinement of the closed state yielded a 4.0-Å-resolution map with well-resolved protomers and axial channel (figs. S2B and S3, A to C). The AAA+ subdomains show side-chain features, enabling an atomic model to be built and refined by using a homology model from the bacterial ortholog ClpB (*11*) (Fig. 1C and fig. S3, D and E). The AAA+ domains (protomers designated P1 to P6) form a near-symmetric closed double ring (Fig. 1D). Protomers P2 to P5 are identical [root mean square deviation (RMSD) = 2 Å], whereas the two mobile protomers, P1 and P6, each adopt different conformations (Fig. 1E and fig. S3F). The outside hexamer diameter is ~115 Å (compared to 125 Å for the open state), and density for the AAA+ domains surround a ~10-Å-wide axial channel. Notably, the channel is partially occluded by a continuous, 80 Å strand of density that, on the basis of the molecular model, is an unfolded portion of the substrate, casein (Fig. 1F).

Tyr pore-loop contacts along substrate

In the closed state, pore-loop strands from both AAA+ domains become ordered compared to Hsp104–AMP-PNP (*9*) and other structures (*11*, *12*) and contact substrate in a right-handed spiral arrangement (Fig. 2A and fig. S4). These regions are among the most highly resolved (<4.0 Å, fig. S3C), indicating bona fide interactions critical for translocation. The casein sequence could not be determined from the density; therefore, a strand of 26 Ala residues was modeled. Hsp104 translocates unfolded polypeptides in the presence of ATP-γ-S (*8*); therefore, the pore loop–substrate interactions likely adopt a fixed register during translocation. Alternatively, a specific region of casein may be uniformly trapped in the channel. Substrate contacts are made by five protomers (P1 to P5), whereas protomer P6 breaks the helical arrangement and makes no direct contact (Fig. 2A and fig. S4). Substrate density is not observed outside the channel, and thus, nontranslocated portions of casein are likely disordered.

Conserved pore-loop tyrosines 257 and 662 in protomers P1 to P5 directly contact substrate, potentially via the aromatic rings, which are positioned ~4 to 5 Å away from the backbone (Fig. 2B). Together with conserved V663 in NBD2 (V, valine), these residues contribute most of the substrate interactions in the channel (fig. S4). Additional loops (residues 291 to 297 for NBD1 and residues 645 to 651 for NBD2) are also ordered and adjacent to the substrate, and K649 and Y650 for P2 and P4 appear to make contact (K, lysine; Y, tyrosine) (Fig. 2, A and B).

The pore loops are separated by ~6 to 7 Å along the channel, making contact with approximately every second amino acid of the substrate (Fig. 2C). K256 and K258 in NBD1, which flank Y257,

[1]Department of Biological Chemistry, Life Sciences Institute, University of Michigan, Ann Arbor, MI 48109, USA. [2]Graduate Program in Chemical Biology, Life Sciences Institute, University of Michigan, Ann Arbor, MI 48109, USA. [3]Department of Biochemistry and Biophysics, Perelman School of Medicine at the University of Pennsylvania, Philadelphia, PA 19104, USA. [4]Pharmacology Graduate Group, Perelman School of Medicine at the University of Pennsylvania, Philadelphia, PA 19104, USA. [5]Biochemistry and Molecular Biophysics Graduate Group, Perelman School of Medicine at the University of Pennsylvania, Philadelphia, PA 19104, USA. [6]Chemistry Department of Brooklyn College and Ph.D. Programs in Chemistry, Biochemistry, and Biology, Graduate Center of the City University of New York, New York, NY 10016, USA.
*These authors contributed equally to this work.
†Corresponding author. Email: dsouth@umich.edu

Downloaded from http://science.sciencemag.org/ on July 20, 2017

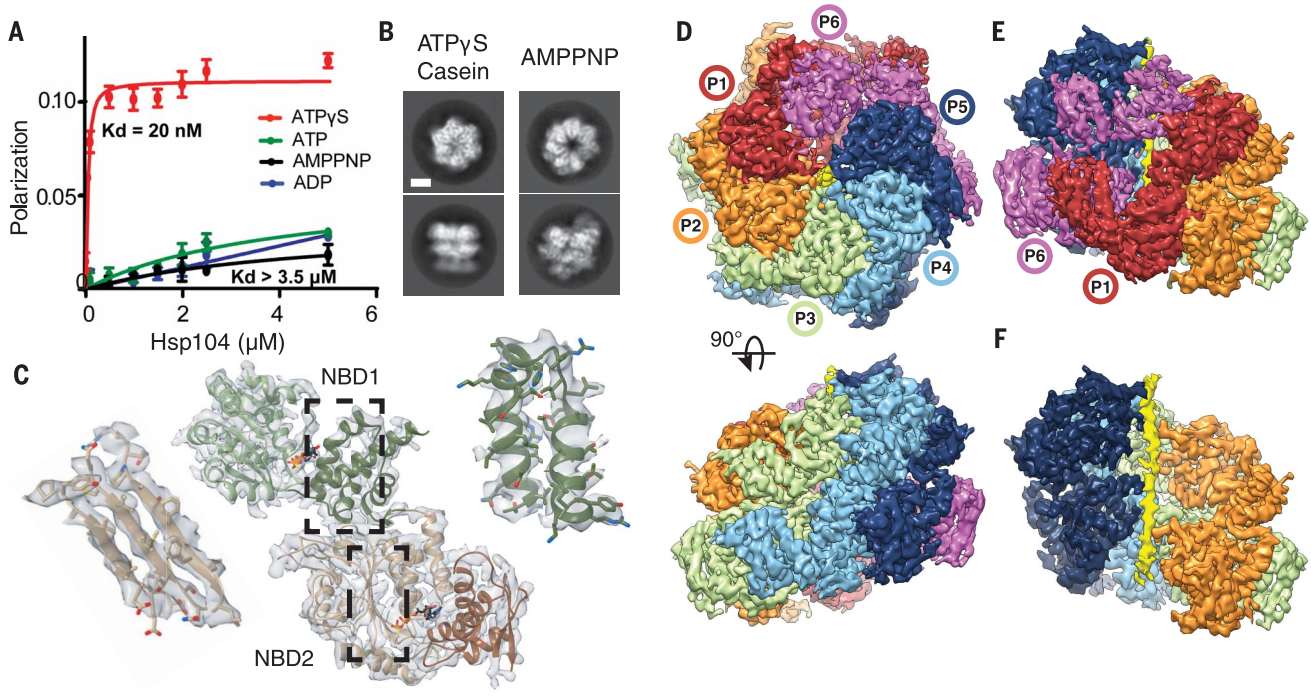

Fig. 1. Substrate-bound Hsp104:casein closed complex. (**A**) FITC-casein binding analysis, measured by fluorescence polarization in the presence of: ATP-γ-S (red), ATP (green), AMP-PNP (black), and ADP (blue) (values = mean ± SD, *n* = 3). (**B**) Representative top- and side-view 2D class averages comparing the Hsp104–ATP-γ-S:casein closed state and Hsp104–AMP-PNP open state (*9*) (scale bar equals 50 Å). (**C**) Atomic model and segmented map of the AAA+ small (NBD1, green) and large (NBD2, brown) subdomains. (**D**) Final reconstruction of Hsp104:casein segmented by protomers (P1 to P6) and substrate (yellow). (**E**) Side view of the mobile protomer face (P1 and P6). (**F**) Channel view showing substrate polypeptide density (yellow).

project toward neighboring loops, possibly stabilizing the spiral arrangement. Protomers P1 and P5 comprise the lowest and highest contact sites with the substrate and are separated by ~26 Å along the channel axis. Protomer P6 is between these sites but disconnected from the substrate; its NBD1 pore loop is 13 Å away, whereas its NBD2 pore loop was less resolved and unable to be modeled (Fig. 2C). Overall, this structure reveals that substrate interactions are mediated almost entirely by the conserved Tyr residues, establishing their direct role in coordinating substrate during translocation (*1*, *2*).

Ratchet-like states of protomers

In addition to the closed state, our 3D-classification analysis identified an extended conformation of Hsp104:casein (fig. S2D). Further classification and refinement resulted in a 4.1 Å resolution map from which an atomic model was determined (Fig. 3A and figs. S2B and S5, A and B). The structure reveals a substrate-bound hexamer with a different arrangement of the mobile protomers P1 and P6, which show distinct flexibility in the NBD1 and NBD2, respectively (Fig. 3A and fig. S5, C and D). Protomers P2 to P5 are identical to the closed state (RMSD = ~0.8 Å), and density for the polypeptide substrate is slightly extended at the top of the channel but is overall similar and localizes to the same region (fig. S5E).

The closed- and extended-state conformational differences for P1 and P6 are substantial (RMSD = 13.7 and 11.5 Å, respectively) and involve rotations of P1-NBD1 and P6-NBD2 (Fig. 3B and fig. S6A). P6 rotates toward the channel axis, and the pore loops become well ordered and directly contact substrate. The P6 pore-loop tyrosines, Y257 and Y662, directly contact substrate similarly as the other protomers (Fig. 3C). Conversely, P1-NBD2 rotates counterclockwise, releasing its interaction with P6 to contact P2-NBD2 but maintaining contact with the substrate (Fig. 3B).

Notably, P6-Y257 becomes positioned at the topmost contact site along the polypeptide, advancing interactions by two amino acids (~7 Å) compared with P5-Y257 (Fig. 3D and fig. S6B). These changes bring P6 pore loops in register to form a two-turn right-handed spiral of contacts. Each pore loop rotates ~60° and rises ~6 to 7 Å, enabling evenly spaced Tyr-substrate interactions across a 74 Å length of the channel. Together, the extended and closed states reveal a ratchet-like conformational change of the hexamer that yields a two–amino acid translocation step (movie S1). Although other conformations may exist that were not resolved, the extended and closed states predominate the data set (fig. S2D); therefore, these changes are likely critical for orchestrating substrate-binding and -release steps during translocation.

Coordinated nucleotide pockets

NBD1 and NBD2 nucleotide pockets were examined to determine how nucleotide state is coupled to substrate interactions. P3 to P5 nucleotide pockets are identical, with well-resolved density and a bound ATP-γ-S (fig. S7A). In NBD1, R334 (R, arginine) from the clockwise neighboring protomer contacts the γ-phosphate, establishing this residue as the Arg finger (*13*). R333 is adjacent to the α- and β-phosphates, acting potentially as a sensor residue considering that the NBD1 does not contain a cis sensor 2 motif (*3*). In the NBD2 pocket, the Arg finger, R765, interacts with the γ-phosphate, whereas the sensor 2, R826 in the cis protomer, is positioned adjacent to the α- and β-phosphates (fig. S4A). Thus, for P3 to P5, which make well-defined contacts with the substrate in both states, NBD1 and NBD2 are primed for ATP hydrolysis.

Conversely, the mobile protomer (P6, P1, and P2) NBDs (fig. S7B) are in different active and inactive configurations based on the position of Arg fingers and nucleotide density. For the P6 protomer, both NBDs appear inactive in the closed state (Fig. 4A) with P5-R334 ~12 Å away and P5-R765 ~6 Å away from the respective NBD1 and NBD2 γ-phosphate in P6. By contrast, both P5-R334 and P5-R765 in the extended state are identified to contact the respective γ-phosphates directly, indicating that these sites are in an active configuration. Notably, the closed-to-extended conformational change results in both nucleotide-pocket activation and substrate contact by P6 (Fig. 3B).

P1 contacts substrate at the lowest position in the hexamer and appears inactive in both states (Fig. 4A). In the closed state, P6-R334 is ~11 Å away and P6-R765 is ~21 Å away from the respective γ-phosphate in P1. These Arg residues are

Downloaded from http://science.sciencemag.org/ on July 20, 2017

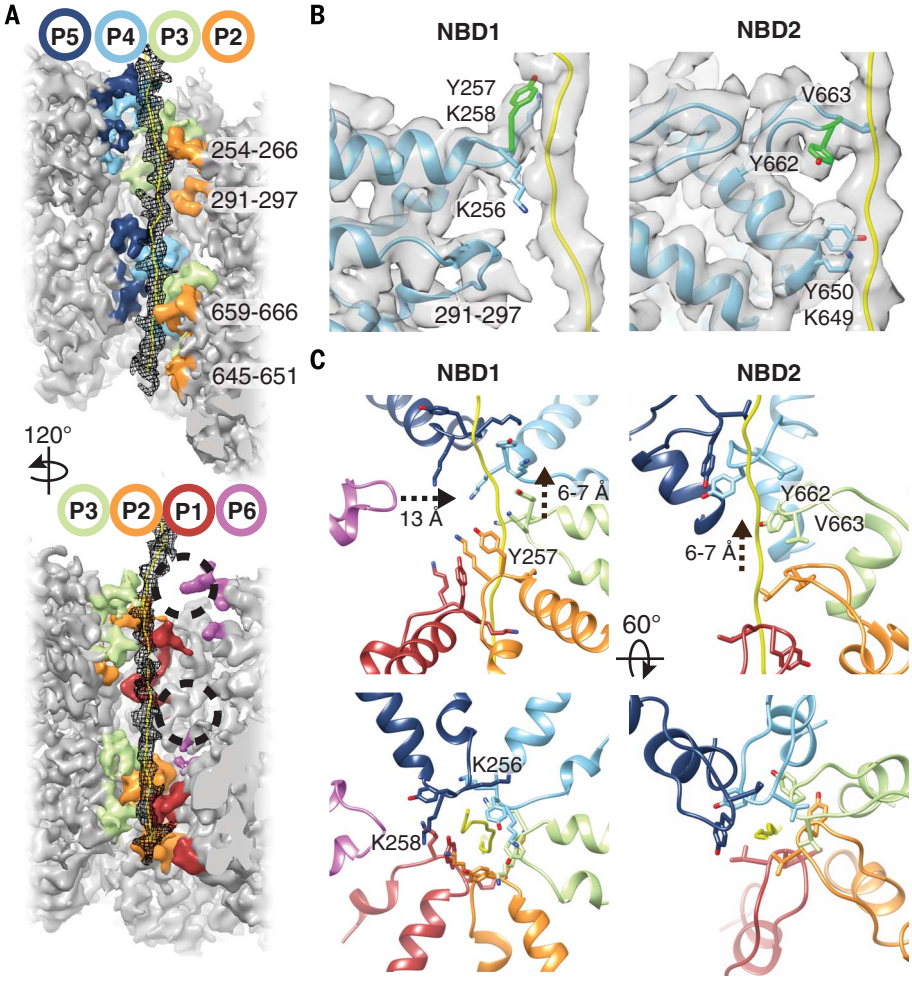

Fig. 2. Structural basis for substrate binding in the axial channel. (**A**) Channel view of the map showing the extended poly-Ala strand modeled as the substrate (mesh) and pore loops with residues indicated. The P6 pore-loop regions not contacting substrate are indicated (circles). (**B**) Model and cryo-EM density showing P4 pore loop–substrate interactions mediated by Y257 (green) in the NBD1 and Y662 (green) and V663 in the NBD2, as well as additional, noncanonical pore loops that include residues K649 and Y650. (**C**) Spiral arrangement of the NBD1 and NBD2 canonical pore loops for P1 to P5 contacting substrate and the disconnected position of the P6-NBD1 pore loop.

further separated from the nucleotide pockets in the extended state, with R333, R334, and R765 more than 30 Å away (Fig. 4A). For P2, NBD1 is in an active configuration in both states. However, P2-NBD2 switches from inactive in the closed state to active in the extended state because of the P1-NBD2 conformational change that brings R765 adjacent the γ-phosphate (Fig. 4A). Finally, on the basis of difference maps, density for nucleotide is present in all sites but appears reduced at certain sites: NBD1 in P6 and P1 for the closed state and NBD2 in P1 for both states, indicating partial occupancy or a posthydrolysis state (fig. S7C).

The NBD states, along with substrate interactions, are depicted in a schematic to explain how active-site rearrangements and the closed-to-extended conformational changes drive substrate translocation (Fig. 4B). In the closed state, substrate is bound by five protomers with four NBD1 sites and three NBD2 sites in an active (ATP) configuration. By contrast, in the extended state, substrate is bound by six protomers with five NBD1 sites and five NBD2 sites in an active state. Importantly, the "off" protomer (P6) that is unbound to substrate in the closed state becomes active in the extended state and binds substrate at the next position. The protomer counterclockwise from this position is in the lowest "down" position (P1) and remains inactive in both states, but undergoes a rotation in the extended state that activates NBD2 of the neighboring protomer.

These results suggest a rotary-type translocation mechanism whereby four protomers remain bound to substrate in a similar configuration with the NBDs primed for hydrolysis, while two protomers at the transition site between the lowest and highest position undergo conformational changes that alter substrate interactions. Given the right-handed spiral of pore loops, position of the "up" and "down" protomers, and NBD1 to NBD2 direction of translocation, peptide movement could occur through a counterclockwise cycling of these closed and extended states. On the basis of this model, the inactive protomer in the down position could release substrate and reengage in the up position, thereby advancing translocation by a two–amino acid step. Transmitting these changes counterclockwise would enable the hexamer to advance processively along the polypeptide during translocation (movie S2). Some variability in the step size, potentially to accommodate bulky residues, could be achieved by conformational changes in the extended-state protomer in the up position that shift its pore-loop contact. These results parallel the right-handed substrate interactions and rotary-driven hydrolysis models for DNA and RNA helicases, including AAA+ (E1, DnaA, and MCM) (*3*, *14*, *15*) and RecA (Rho) (*16*) families. Thus, this ratcheting mechanism may be conserved among many ATP-driven translocases.

Allosteric control by the MD

The Hsp104–AMP-PNP (*9*) structure revealed an open-spiral conformation that is substantially different from the closed, substrate-bound states characterized here. Furthermore, a MD-NBD1 interaction was identified that suggested an allosteric control mechanism. To further explore the MD and the role of nucleotide in the Hsp104 conformational cycle, we determined the cryo-EM structure of Hsp104 incubated with ADP to 5.6 Å resolution (Fig. 5A and fig. S8, A to C). The reconstruction reveals an identical AAA+ arrangement compared to Hsp104–AMP-PNP (RMSD = 2.5 Å) involving a left-handed spiral architecture defined by a ~10 Å rise per protomer and a heteromeric AAA+ interaction between P6-NBD1 and P1-NBD2.

The MD is resolved for three protomers (P3 to P5) and identified to be in a crisscross equatorial arrangement stabilized by contacts between the first (L1) and third (L3) helices (Fig. 5B). This arrangement is similar to previous structures (*11*, *12*, *17*) but markedly different to the Hsp104–AMP-PNP structure, in which the same MD L1 region makes contact across the NBD1 of the clockwise protomer (Fig. 5C). Comparison of these ATP- and ADP-state MD conformations reveals a substantial, ~30° rotation around position 409 at the MD-NBD1 junction (fig. S8D and movie S3). Although hexamers exclusively bound to ATP or ADP are likely rare in vivo, these data reveal that the MD adopts two nucleotide-specific conformations that reflect pre- and posthydrolysis states.

Sites that comprise the MD-MD interactions in Hsp104-ADP are critical for function (*4*, *5*, *12*, *13*). However, the AMP-PNP–specific MD L1–NBD1 interaction has not been characterized. Therefore, single charge-reversal mutations were introduced to disrupt three putative L1-NBD1 salt bridges (*9*): E412-R194, E427-R353, and D434-R366 (E, glutamic acid; D, aspartic acid) (Fig. 5C). These mutants exhibit robust ATPase activity (fig. S8E). However, they are unable to reactivate

Downloaded from http://science.sciencemag.org/ on July 20, 2017

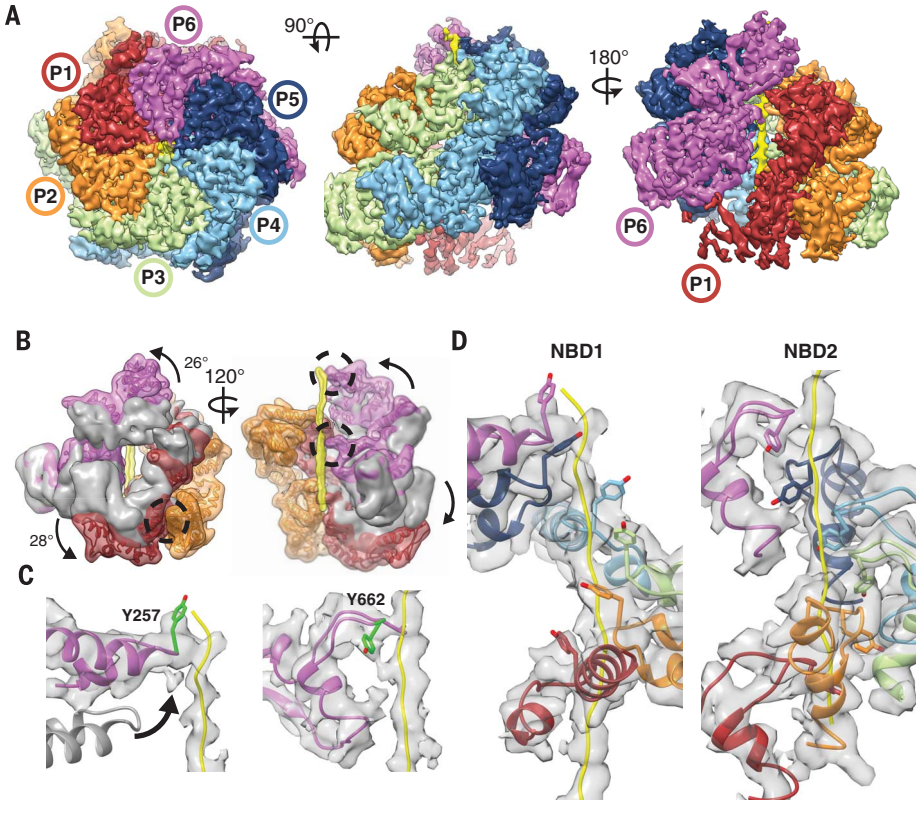

Fig. 3. Hsp104:casein extended-state conformation advances substrate contacts. (**A**) Cryo-EM reconstruction of Hsp104:casein identifying substrate (yellow) and an extended conformation of protomers P1 and P6. (**B**) Filtered map of P1 (red) and P6 (magenta) overlaid with the corresponding closed-state protomers (gray) after alignment to P4 in the hexamer. NBD conformational changes (arrows) resulting in extended-state interactions (black circles) with substrate (yellow) and the P2-NBD2 (orange) are shown. (**C**) Model and map of the P6-NBD1 and -NBD2 pore loops showing change in the pore-loop position (arrow) compared to the closed state (gray) for NBD1 and substrate contact by Y257 and Y662 (green). (**D**) Model and map of the NBD1 and NBD2 P1 to P6 spiral of pore loop–substrate interactions.

denatured firefly luciferase aggregates in vitro (Fig. 5D) or confer thermotolerance in vivo (fig. S8E), supporting a functional role for the L1-NBD1 interaction.

To determine MD conformations in the casein-bound complex, additional 3D subclassification analysis and refinement were performed on the Hsp104 closed-state data without applying a mask (fig. S9A). Three classes with distinct MD arrangements were identified: MD class 1, class 2, and class 3, which refined to 6.7 to 6.9 Å (Fig. 5E and fig. S9B). For these maps, the AAA+ core and substrate density are identical to the closed-state structure. In the MD class 1, density corresponding to the MD coiled coil is identified for four protomers (P1, P2, P5, and P6), revealing an ADP-state, criss-cross arrangement around the P6 to P1 mobile-protomer face (Fig. 5E). Notably, the N-terminal domains (NTDs) for all protomers are also resolved in this class, revealing that they interact together in an alternating, triangular arrangement with the polypeptide strand oriented asymmetrically in the channel, toward the P3 and P5 NTDs (fig. S10).

For MD class 2, density corresponding to MD helices L1 and L2 is identified for protomers P3 to P5, revealing that L1 is positioned across the clockwise protomer, which indicates an ATP-state conformation (Fig. 5E). For class 3, both MD conformations are identified: P1, P5, and P6 adopt the ADP state, while P3 and P4 are in the ATP state (Fig. 5E). This classification captures specific MD conformations that are in specific agreement with our analysis of the nucleotide pockets (Fig. 4). Thus, in an actively translocating hexamer, MD conformational changes likely propagate around

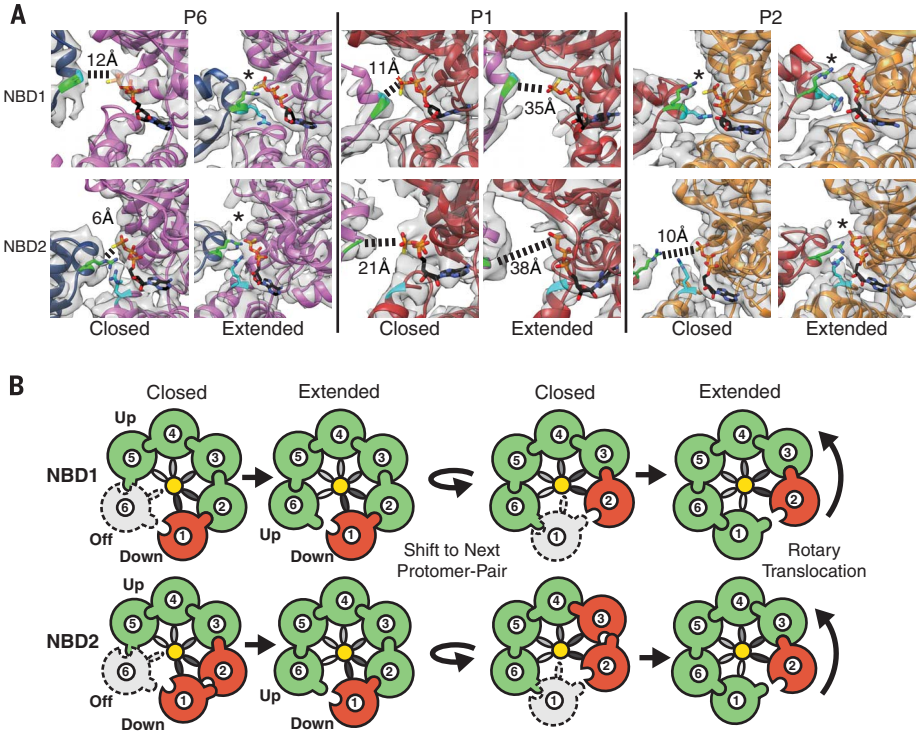

Fig. 4. Extended-state activation of the nucleotide pockets is coupled to translocation. (**A**) Map and model of the P6, P1, and P2 nucleotide pockets. Arg fingers NBD1-R334 and NBD2-R765 are shown (green) with γ-phosphate contact indicated (*) for the active sites and distances shown for the inactive sites. Sensor 2 residues NBD1-R333 and the NBD2-R826 are shown (cyan). (**B**) Rotary translocation model showing closed-to-extended states resulting in active (green), inactive (red), and unbound or inactive (gray dash) states of the NBDs. Pore-loop spiral (gray gradient) is shown contacting substrate (yellow). Arg-finger contact and NBD activation is depicted by the interlocking contact.

Downloaded from http://science.sciencemag.org/ on July 20, 2017

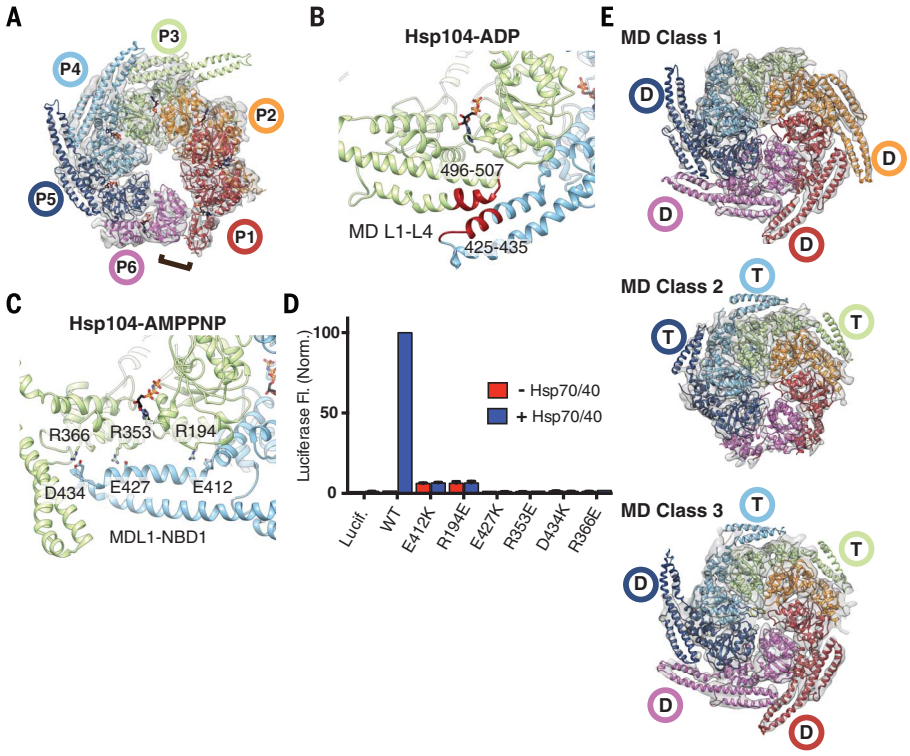

Fig. 5. Nucleotide-specific MD conformations identified around the substrate-bound hexamer. (**A**) Cryo-EM map and model of Hsp104-ADP in the open-spiral conformation, with the NBD1-NBD2 heteromeric interaction shown (bracket). (**B**) MD-MD (L1-L3) interaction interface identified in the Hsp104-ADP reconstruction (red). (**C**) MD L1–NBD1 interaction identified in the Hsp104–AMP-PNP structure (*9*), showing putative salt-bridge contacts analyzed by mutagenesis. (**D**) Luciferase reactivation measured by fluorescence after incubation with Hsp104 wild type (wt) or indicated mutants in the absence (red) or presence (blue) of an Hsp70/40 system. Values are normalized to wt + Hsp70/40 and represent the mean ± SD (n = 4). (**E**) Final reconstructions and models of Hsp104:casein after classification analysis identifying the ADP-state (D) or ATP-state (T) MD conformation.

the hexamer in accordance with nucleotide state. The MD could function to lock the ATP state for protomers that are in contact with substrate (P2 to P5) and transition to a posthydrolysis release state toward the mobile face, thereby allosterically tuning the closed and extended conformational changes that advance substrate.

NBD1-driven rearrangement engages substrate

To determine how the open and closed states may function together, cryo-EM data sets of wild-type and mutant Hsp104 incubated with different nucleotides were analyzed by 2D and 3D classification methods (Fig. 6A and fig. S11A). As expected, AMP-PNP and ADP data sets classify with 100% of the data matching the open conformation. With ATP incubations, alone and with substrate, Hsp104 primarily adopts the open conformation (>80%); however, a notable fraction (10 to 20%) are in the closed state. A 3D reconstruction of the Hsp104-ATP structure was determined to 6.7 Å and is identical to the AMP-PNP– and ADP-bound structures (cross-correlation = 0.98) (fig. S11B). Thus, during active hydrolysis (fig. S8E), the open state is favored; however, both conformations exist in equilibrium. With ATP-γ-S, nearly 80% of hexamers are in the closed state (Fig. 6A), which increases to 100% with casein, demonstrating that ATP-γ-S and substrate together trigger complete conversion to the closed state.

The sensor 1 ATPase mutants (*18*), T317A in NBD1 and N728A in NBD2 (T, threonine; A, alanine; N, asparagine), were investigated to determine the role of NBD1 and NBD2 function (Fig. 6A). In contrast to wild type, T317A incubated with ATP or ATP-γ-S classifies with 100% matching the open state, indicating that a hydrolysis-active NBD1 promotes the closed conformation. Conversely, ~80 and 60% of N728A hexamers match the closed state in the presence of ATP and ATP-γ-S, respectively. In casein-binding experiments, N728A binds with high affinity (K_d ~ 33 nM); in contrast, wild type and T317A show weak binding (K_d > 2 μM) (Fig. 6B) in the presence of ATP. With ATP-γ-S, both wild type and N728A bind with a high affinity (K_d ~ 16 to 20 nM), whereas T317A has a reduced affinity in comparison (K_d ~ 1.4 μM) (Fig. 6C). Thus, Hsp104 exists in an open-to-closed conformational equilibrium that is differentially controlled by NBDs. Hydrolysis by NBD1 promotes the closed state, but hydrolysis by NBD2 favors the open state. Substrate binding and the open-to-closed conformational change are coupled and likely driven by NBD1 function, whereas NBD2 may be important for substrate-release steps.

Massive conformational changes are required to transition between the open and closed states (Fig. 6D and movie S4). In the open state, protomer P1 is in the topmost position, and the hexamer adopts a left-handed spiral with P6 ~ 50 Å below, along the axial channel. Upon conversion to the closed state, P6 shifts by ~65 Å and rotates toward the channel by ~60° (fig. S12), resulting in a right-handed spiral and a channel that has narrowed by ~10 Å. Considering that substrate interactions and hydrolysis by NBD1 are critical for the closed state (Fig. 6, A to C), we propose that this large conformational change drives substrate-binding and -release steps of the cycle (Fig. 6D). When the conformational change is modeled with substrate, nearly 30 residues can be translocated into the channel. Additionally, similar open "lock-washer" conformations are populated by other translocases (*19*–*22*), which may represent a conserved off state.

Disaggregation involves nonprocessive and processive mechanisms (*23*, *24*). Cycling between the open and closed states may enable nonprocessive bind and release "pulling" events. Alternatively, the two different substrate-bound states suggest a processive mechanism whereby two protomers undergo ratchet-like conformational changes that enable substrate-binding and -release steps to occur while the hexamer remains engaged. This rotary-like mechanism could drive disaggregation when coupled to stepwise cycles of ATP hydrolysis around the ring (movie S2). Such a cooperative mechanism could enable dissolution of more stable aggregates or amyloids (*23*). Although this mechanism contrasts with stochastic models proposed for ClpX (*1*), Hsp104 may exhibit different conformational cycles tuned to different substrates (*23*). Notably, both extended and closed states reveal a precise 6 to 7 Å separation of the pore loop–substrate contacts. A two–amino acid step involving conformational changes at the spiral interface would continually maintain this register during translocation. This pore-loop spacing is observed in related AAA+ rings (*25*–*27*) and represents a conserved feature of translocases. Although additional states are likely involved, our structures reveal a substrate-dependent structural plasticity for Hsp104, which could enable

Downloaded from http://science.sciencemag.org/ on July 20, 2017

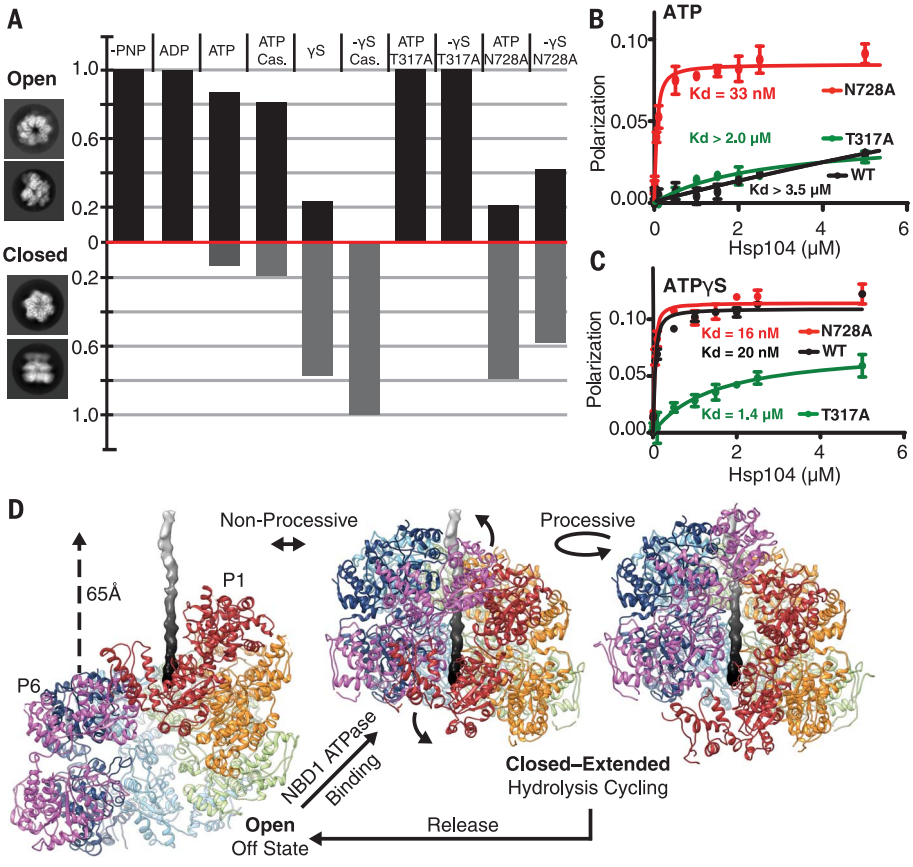

Fig. 6. Nucleotide-state and NBD function in the open-closed conformations and model for the disaggregation cycle. (**A**) The fraction of open and closed conformations, determined by 3D classification analysis, is shown for wild-type Hsp104 and sensor 1 ATPase mutants (T317A in NBD1 and N728A in NBD2) after incubation with indicated nucleotides and substrate (-PNP stands for AMP-PNP; -γ-S stands for ATP-γ-S). (**B** and **C**) FITC-casein (60 nM) binding to Hsp104 wild type (black) and mutants T317A (green) and N728A (red) in the presence of (2 mM) ATP (B) or ATP-γ-S (C). Values represent mean ± SD (n = 3). (**D**) Proposed models for nonprocessive and processive modes of translocation involving open-to-closed conformational change upon substrate engagement and release and ratchet-like open-to-extended protomer changes that occur around the hexamer during cycles of ATP hydrolysis.

adaptable mechanisms of protein disaggregation (*2*, *23*).

REFERENCES AND NOTES

1. A. O. Olivares, T. A. Baker, R. T. Sauer, *Nat. Rev. Microbiol.* **14**, 33–44 (2016).
2. E. A. Sweeny, J. Shorter, *J. Mol. Biol.* **428**, 1870–1885 (2016).
3. J. P. Erzberger, J. M. Berger, *Annu. Rev. Biophys. Biomol. Struct.* **35**, 93–114 (2006).
4. M. E. Jackrel *et al.*, *Cell* **156**, 170–182 (2014).
5. Y. Oguchi *et al.*, *Nat. Struct. Mol. Biol.* **19**, 1338–1346 (2012).
6. J. Lee *et al.*, *Proc. Natl. Acad. Sci. U.S.A.* **110**, 8513–8518 (2013).
7. R. Lum, J. M. Tkach, E. Vierling, J. R. Glover, *J. Biol. Chem.* **279**, 29139–29146 (2004).
8. P. Tessarz, A. Mogk, B. Bukau, *Mol. Microbiol.* **68**, 87–97 (2008).
9. A. L. Yokom *et al.*, *Nat. Struct. Mol. Biol.* **23**, 830–837 (2016).
10. S. M. Doyle *et al.*, *Nat. Struct. Mol. Biol.* **14**, 114–122 (2007).
11. S. Lee *et al.*, *Cell* **115**, 229–240 (2003).
12. M. Carroni *et al.*, *eLife* **3**, e02481 (2014).
13. P. Wendler *et al.*, *Cell* **131**, 1366–1377 (2007).
14. E. J. Enemark, L. Joshua-Tor, *Nature* **442**, 270–275 (2006).
15. F. Abid Ali *et al.*, *Nat. Commun.* **7**, 10708 (2016).
16. N. D. Thomsen, J. M. Berger, *Cell* **139**, 523–534 (2009).
17. A. Heuck *et al.*, *eLife* **5**, e21516 (2016).
18. D. A. Hattendorf, S. L. Lindquist, *EMBO J.* **21**, 12–21 (2002).
19. A. Y. Lyubimov, A. Costa, F. Bleichert, M. R. Botchan, J. M. Berger, *Proc. Natl. Acad. Sci. U.S.A.* **109**, 11999–12004 (2012).
20. E. Skordalakes, J. M. Berger, *Cell* **114**, 135–146 (2003).
21. P. Śledź *et al.*, *Proc. Natl. Acad. Sci. U.S.A.* **110**, 7264–7269 (2013).
22. M. Zhao *et al.*, *Nature* **518**, 61–67 (2015).
23. M. E. DeSantis *et al.*, *Cell* **151**, 778–793 (2012).
24. T. Li *et al.*, *Biochem. J.* **470**, 39–52 (2015).
25. M. Wehmer, E. Sakata, *Int. J. Biochem. Cell Biol.* **79**, 437–442 (2016).
26. S. E. Glynn, A. Martin, A. R. Nager, T. A. Baker, R. T. Sauer, *Cell* **139**, 744–756 (2009).
27. M. E. Matyskiela, G. C. Lander, A. Martin, *Nat. Struct. Mol. Biol.* **20**, 781–788 (2013).

ACKNOWLEDGMENTS

We thank J. Smith and L. Rice for discussion of the manuscript and F. DiMaio for help with Rosetta. A.L.Y. is supported by an American Heart Association (AHA) predoctoral fellowship. M.E.J. is supported by a Target Amyotrophic Lateral Sclerosis (ALS) Springboard Fellowship. E.A.S. is supported by an AHA predoctoral fellowship and NIH grant T32GM008275. E.C. is supported by NIH grant T32GM008076. M.P.T. is supported by NIH grants K12GM081259 and K22NS09131401. K.L.M. is supported by an NSF Graduate Research Fellowship (DGE-1321851). J.S. is supported by NIH grant R01GM099836, a Muscular Dystrophy Association Research Award (MDA277268), the Life Extension Foundation, the Packard Center for ALS Research at Johns Hopkins University, and Target ALS. D.R.S. is supported by NIH grants R01GM109896, R01GM077430, and R01GM110001A. Cryo-EM maps and models are deposited in the Electron Microscopy and Protein Data Banks (EMDB and PDB, respectively): Hsp104:casein closed state (EMDB: 8697, PDB: 5VJH), extended state (EMDB: 8746, PDB: 5VYA), and middle-domain conformation (EMDB: 8745, PDB: 5VY9); and Hsp104-ADP (EMDB: 8744, PDB: 5VY8).

SUPPLEMENTARY MATERIALS

www.sciencemag.org/content/357/6348/273/suppl/DC1
Materials and Methods
Figs. S1 to S12
Tables S1 and S2
Movies S1 to S4
References (*28*–*43*)

5 March 2017; accepted 31 May 2017
Published online 15 June 2017
10.1126/science.aan1052

Downloaded from http://science.sciencemag.org/ on July 20, 2017

Science

Ratchet-like polypeptide translocation mechanism of the AAA+ disaggregase Hsp104

Stephanie N. Gates, Adam L. Yokom, JiaBei Lin, Meredith E. Jackrel, Alexandrea N. Rizo, Nathan M. Kendsersky, Courtney E. Buell, Elizabeth A. Sweeny, Korrie L. Mack, Edward Chuang, Mariana P. Torrente, Min Su, James Shorter and Daniel R. Southworth

Science **357** (6348), 273-279.
DOI: 10.1126/science.aan1052originally published online June 15, 2017

Untangling aggregates one step at a time

Conserved AAA+ protein complexes exploit adenosine triphosphate hydrolysis to unfold and disaggregate their substrates in response to cell stress, but exactly how they do this has been unclear. Gates *et al.* determined high-resolution cryo-electron microscopy structures of the Hsp104 disaggregase bound to an unfolded polypeptide substrate in its channel. The structures reveal substrate interactions and two different translocation states. Hsp104 undergoes conformational changes that drive movement along the substrate by two-amino-acid steps. These states help explain how this molecular machine can solubilize protein aggregates and amyloids.

Science, this issue p. 273

ARTICLE TOOLS http://science.sciencemag.org/content/357/6348/273

SUPPLEMENTARY MATERIALS http://science.sciencemag.org/content/suppl/2017/06/14/science.aan1052.DC1

REFERENCES This article cites 43 articles, 10 of which you can access for free
http://science.sciencemag.org/content/357/6348/273#BIBL

PERMISSIONS http://www.sciencemag.org/help/reprints-and-permissions

Use of this article is subject to the Terms of Service

Science (print ISSN 0036-8075; online ISSN 1095-9203) is published by the American Association for the Advancement of Science, 1200 New York Avenue NW, Washington, DC 20005. 2017 © The Authors, some rights reserved; exclusive licensee American Association for the Advancement of Science. No claim to original U.S. Government Works. The title *Science* is a registered trademark of AAAS.

Downloaded from http://science.sciencemag.org/ on July 20, 2017

www.sciencemag.org/cgi/content/full/science.aan1052/DC1

Supplementary Materials for

Ratchet-like polypeptide translocation mechanism of the AAA+ disaggregase Hsp104

Stephanie N. Gates, Adam L. Yokom, JiaBei Lin, Meredith E. Jackrel, Alexandrea N. Rizo, Nathan M. Kendsersky, Courtney E. Buell, Elizabeth A. Sweeny, Korrie L. Mack, Edward Chuang, Mariana P. Torrente, Min Su, James Shorter, Daniel R. Southworth*

*Corresponding author. Email: dsouth@umich.edu

Published 15 June 2017 on *Science* First Release
DOI: 10.1126/science.aan1052

This PDF file includes:

Materials and Methods
Figs. S1 to S12
Tables S1 and S2
Captions for Movies S1 to S4
References

Other Supplementary Materials for this manuscript includes the following:
(available at www.sciencemag.org/cgi/content/full/science.aan1052/DC1)

Movies S1 to S4

Materials and Methods

Purification, Fluorescence Polarization, and Size Exclusion Chromatography.

All Hsp104 variants were generated using QuikChange site-directed mutagenesis (Agilent) and confirmed by DNA sequencing. Hsp104, $Hsp104^{T317A}$, $Hsp104^{N728A}$, $Hsp104^{E412K}$, $Hsp104^{R194E}$, $Hsp104^{E427K}$, $Hsp104^{R353E}$, $Hsp104^{D434K}$, and $Hsp104^{R366E}$ were purified as described(*4, 28*). Hsc70 and Hdj2 were from Enzo Life Sciences. For fluorescence polarization studies, $Hsp104^{WT}$, $Hsp104^{T317A}$, or $Hsp104^{N728A}$ were exchanged into 40 mM Hepes-KOH pH 7.4, 20 mM $MgCl_2$, 150 mM KCl, 10% Glycerol (v/v), 2 mM 2-Mercaptoethanol. To assess FITC-casein binding, FITC-casein (60 nM) was incubated with increasing concentrations (0-5μM hexameric) of Hsp104, $Hsp104^{T317A}$, or $Hsp104^{N728A}$ with 2 mM of the indicated nucleotide for 10 min at 25°C. For the ATP condition, an ATP regeneration system (5mM creatine phosphate and 0.125μM creatine kinase) was also included to maintain the ATP concentration. Fluorescence polarization was measured (excitation 470 nm, emission 520 nm) using a Tecan Infinite M1000 plate reader. The binding isotherms were analyzed using MicroMath Scientist 3.0. Parameters: IndVars=Xt; DepVars=P; Params: Bmax, K, Mtot; Xbar=Xf / (K + Xf); Xt=Xf+Xbar*Mtot; P=Bmax *Xbar; 0<Xf<Xt (P represents the fluorescence polarization values, Xt represents total $[Hsp104]_6$, Xf represents free $[Hsp104]_6$, Xbar represents degree of binding, and Mtot represents total [casein]).

Size exclusion chromatography (SEC) analysis and purification was performed by incubating wildtype Hsp104 (20 μM) with nucleotide (ATP, ATPγS, AMPPNP or ADP at 5 mM) in the presence or absence of FITC-casein (#C0528, Sigma) in buffer containing: 20 mM Hepes (pH=7.5), 50 mM KCl, 10 mM $MgCl_2$, 1 mM DTT. Samples were subsequently separated using a Superose 6 PC 3.2/30 column (GE Healthcare) in a running buffer containing: 40 mM

Hepes (pH=7.5), 40 mM KCl, 10 mM $MgCl_2$, 1 mM DTT. Fractions were analyzed by SDS-PAGE to confirm the presence of Hsp104 and casein. Of note, SEC analysis of FITC-casein alone (Figure 1B and Fig. S1A) identified a monomer peak, eluting at ~1.7 mL, and a broad oligomer peak, eluting at ~1.2 mL, which is distinguishable from the ATPγS-Hsp104 and ATPγS-Hsp104:casein peaks, which elute at ~1.3 mL. The casein oligomer is attributed to its known polymerization capability(*29*) and appears to be solubilized by Hsp104 considering it is significantly diminished in the presence of Hsp104 (Figure S1). For samples subjected to cryo-EM analysis, excess nucleotide (1mM) was added following fractionation to ensure binding during grid preparations.

Cryo-EM Data Collection and 3D Reconstructions. Protein samples were diluted to ~700μg/mL and applied to glow-discharged C-Flat holey carbon grids (CF-2/1-4C-T, Protochips) following SEC fractionation or incubation with various nucleotides (when casein was not present). Samples were plunge-frozen using a vitrobot (FEI Company) and imaged as indicated (Table S1), on a Titan Krios TEM operated at 300 keV (FEI Company). Images were recorded on a K2 Summit detector (Gatan Inc.) operated in counted mode at 50,000X nominal magnification corresponding to a calibrated 1.00 Å/pixel. Dose fractionated imaging was performed by semi-automated collection methods using UCSF Image 4(*30*). Six second exposures were collected at 100 msec/frame, with a total electron dose of 48 e- per micrograph in 60 frames (Table S1). Whole-frame drift correction was performed via Unblur(*31*), removing the first 2 frames of the data due to the large degree of drift. Dose weighting was applied to frames above a 30-electron total dose.

Micrographs were CTF corrected using CTFFIND4(*32*) in Relion(*33*) and single particles were automatically selected using Appion template picker within the Leginon pipeline(*34*). Templates were determined from the previously published Hsp104:AMPPNP data(*9*). Initial 2D classification was performed to assess data quality and remove contamination and incomplete hexamer particles; this amounted to < 5% of the data for the Hsp104-ATPγS:casein dataset. All 3D classification and refinement steps were performed with Relion(*33*). For the Hsp104-ATPγS:casein data, the refinement scheme and resulting data are depicted (Fig. S2D and Table S1). An initial 3D refinement was performed using the Hsp104-AMPPNP structure(*9*), low pass filtered to 50 Å, as an initial model. The resulting reconstruction was used as the model for refinement using the total dataset, (~460,000 single particles from 3,000 micrographs) (Fig S2D). Although this structure refined to an estimated 3.9 Å (Fig S2B), two protomer sites were identified to be poorly resolved. Therefore, a 10-class 3D classification was performed resulting in the identification of the 'closed' and 'extended' conformations. Extensive combinations of these classes were tested by 3D refinement in order to obtain the highest resolution models. A mask around the AAA+ core, determined with Relion, was imposed during refinement to exclude the flexible NTDs and MDs and improve the resolution. Combining classes 2 and 7 yielded the highest resolution map of the closed conformation (4.0Å) (Figure S2B-D). Additional sub-classifications of the 'closed-state' data (combining classes: 1,2, 5-8, and 10, or classes: 1, 5, 6, 8, 10) were performed, but did not yield improvements to the final map, and no additional conformations were identified. The final map of the extended state, at 4.1 Å resolution, was achieved by combining classes 3, 4 and 9 and performing a sub-classification with 6-classes, followed by refinement of two of the resulting classes (Figure S2D and Table S1). Refinement of the total extended state particles (classes 3,4 and 9) yielded a nearly identical structure at 4.0 Å

resolution however the additional classification and refinement showed improved density for the NBD2 small domain of P1 and the NBD1 of P6.

For the Hsp104-ADP reconstruction (Table S1), ~190,000 particles were automatically picked, as above, and 2D classification was performed to remove any contamination and poorly-resolved particles, resulting in a total of ~125,000 particles. The reconstruction was determined as previously described(*9*), using the Hsp104-AMPPNP map, low pass filtered to 50 Å, as the initial model. 3D classification indicated the data were homogeneous with no additional MD states therefore all the single particles were used in the refinement, resulting in a final model that represents the predominant ADP-bound Hsp104 conformation (Fig. S8A-C).

To resolve the MD conformations in the Hsp104:casein complex, all closed-state data (~231,000 particles) were re-classified into 16 classes and a closed-state map (low-pass filtered to 50 Å) with the MDs and NTDs removed served as the starting model. The 3D classes were grouped by superposition and visual comparison of the MD conformations and then combined for refinement, resulting in three final models (MD Class 1-3) (Fig. S9A-B and Table S1). This approach was performed with the extended-state data; however, the MDs were unable to be clearly resolved for the mobile protomers and thus not refined further. For all final maps, the "Post-processing" procedure was used to generate a soft mask for the two half maps prior to FSC estimation and automated B-factor sharpening was performed with the combined maps (Table S1). The local resolution was estimated using ResMap(*35*) for the unsharpened closed and extended-state maps (Fig. S3C and S5C).

Atomic Modeling. Initial rigid body fitting of a SWISS-MODEL(*36*) homology model based on ClpB (pbd=1qvr) served as the starting structure for model building using the closed-state map.

Sub Domains (NBD1 Large/Small and NBD2 Large/Small) were segmented and rigid body fit using UCSF Chimera's *Fit in Map* function. P4 was selected for initial modeling as it showed the best resolution among protomers. Missing pore loop residues in P4 of the closed model were built de novo using COOT(*37*) and Phenix(*38*). Rosetta Comparative Modeling procedures (described below) were then used for refinement to achieve the complete hexamer model(*39, 40*).

Template models were selected through HHsearch against full-length *S. cerevisiae* Hsp104 sequence. This sequence was threaded onto the initial model, fit by rigid body methods, and the four top-scoring matches were selected using the *partial_thread* tool within Rosetta (pbd=1qvr, 5d4w, 5kne, 1rxg). These templates were set to *template_weight=0.0* within the template mover of Rosetta CM, while our initial model was set to *template_weight=1.0*. Modeling and refinement of P4 was performed as a P3-P4 dimer within a segmented map in order to accurately build the CTD, which was not available in published structures and forms part of the protomer interface. 1000 trajectories were sampled for this P3-P4 dimer and the top 20 models, based on rosetta energy score, were inspected for convergence. An additional template was used to ensure the convergence of the NBD2 pore loop (pdb=4fcv)(*41*), which was added to improve further trajectories of the loop region 639-686. The converged P4 model was rigid body fit into P2,P3, and P5 without change in the NBD1-NBD2 orientation, however both P1 and P6 are in substantially different conformations compared to the P4 model and modeled independently. This was achieved by rigid body-fitting the NBD1 and NBD2 domains using UCSF Chimera and then running trajectories in Rosetta CM for the P1-P6 protomer dimer with an additional 1000 models generated to obtain an accurate final model for P1 and P6. The

extended-state model was determined by docking P2-P5 from the closed state and independently modeling P1 and P6, as above.

The final protomer models were combined into the full hexamer map with ATPyS molecules docked in all 12 NBD pockets. Additional density in the channel was attributed to an unfolded polypeptide from the FITC-casein substrate. The sequence could not be resolved, therefore a poly-Alanine chain (26 and 28 residues for the closed and extended states, respectively) was modeled. The N-terminus was arbitrarily oriented towards NBD2; Hsp104 may translocate either orientation of the substrate in the NBD1-to-NBD2 direction(*10, 18, 42*). To ensure the protomer interfaces were correctly modeled, 400 trajectories were sampled on the full hexamer complex. The 20 best models, which had the lowest energy and best electron density fit, were taken for manual inspection. Models converged well in all areas and the top model was chosen for local relax to ensure proper sidechain rotamer modeling. The final closed and extended models were relaxed into training maps derived from half of the respective data and checked for overfitting by comparing the FSC against the training or test maps (Figure S3D and S5B). All images and movies were generated using UCSF Chimera(*43*).

Open/Closed Conformational Analysis. A specific 3D classification and analysis scheme was performed to determine the fraction of open and closed hexamer populations in the presence of different nucleotides and casein for Hsp104 wildtype, T317A and N728A (Fig. S11 and Table S2). 3D classification was performed for each of the datasets with Relion(*33*) using the MD Class 1 closed-state reconstruction low pass filtered to 30 Å as an initial model. Data were split into 4 classes in order to properly separate the open and closed states and account for poorly-resolved data that did not classify to either state. Both the open and closed-state reconstructions

were tested as initial models but only the closed-state allowed convergence to either conformation in initial test datasets. The resulting maps were fit into the closed- and open-state reconstructions, low pass filtered to 15 Å, using the *Fit in Map* function in Chimera(*43*) to determine the cross-correlation (CC). Maps with a CC value ≥ 0.93 were designated as a match to that state. Maps that compared with a CC value < 0.93 to both the open and closed states were overall poorly resolved, thus the data were not included in subsequent analysis. Notably, top-view projections of the open and closed states show clear distinguishing features (Fig. S6), including clear differences in the channel diameter, therefore 2D classification was performed on all data sets as well to verify proper classification.

ATPase Assay. Hsp104 (0.25μM monomer) WT or mutant was equilibrated in Luciferase Refolding Buffer (LRB: 25 mM HEPES-KOH, pH 7.4, 150 mM KAOc, 10 mM MgAOc, 10 mM DTT) for 15 min on ice and then incubated for 5 min at 25°C in the presence of ATP (1 mM) plus or minus casein (2μM). ATPase activity was assessed by the release of inorganic phosphate, which was determined using a malachite green phosphate detection kit (Innova) (Fig. S8E)

Luciferase Reactivation Assay. To generate aggregated luciferase, firefly luciferase (50 μM) in LRB plus 8 M urea was incubated at 30°C for 30 min. The sample was then rapidly diluted 100-fold into LRB. Aliquots were snap frozen in liquid N_2 and stored at −80°C until use. Aggregated luciferase (50 nM) was incubated with Hsp104 (1 μM monomer), Hsc70 (0.167 μM) and Hdj2 (0.167 μM) plus ATP (5 mM) and an ATP regeneration system (10 mM creatine phosphate, 0.25μM creatine kinase) for 90 min at 25°C. At the end of the reaction, luciferase activity was

assessed with a luciferase assay system (Promega). Recovered luminescence was monitored using a Tecan Infinite M1000 plate reader (Fig. 5D).

Induced Thermotolerance Assay. W303aΔ*hsp104* (MATa, can1–100, his3–11,15, leu2–3,112, trp1–1, ura3–1, ade2–1, hsp104:kanMX4) yeast cells were transformed with a centromeric plasmid, pHSEgc, encoding Hsp104 or indicated variant under the control of the HSP104 promoter. The empty pHSEgc vector served as a negative control. Transformed yeast were grown at 30°C in S-Dextrose-His (SD-His) media to an optical density of OD_{600}=0.6. Cells were incubated at 37°C for 30 min to induce the expression of Hsp104 or the indicated variant and then transferred to 50°C for 0, 20 min or 30 min heat shock. Cells were then transferred to ice for 2 min. To evaluate viability, cells were then diluted 1,000-fold in ice-cold SD-His and plated on SD-His. Colonies were counted using an aCOLyte automated colony counter (Synbiosis) after growth at 30°C for 2 days (Fig. S8F). Immunoblot analysis showed that each Hsp104 variant was expressed at a similar level under equivalent conditions.

Supplementry Figure S1

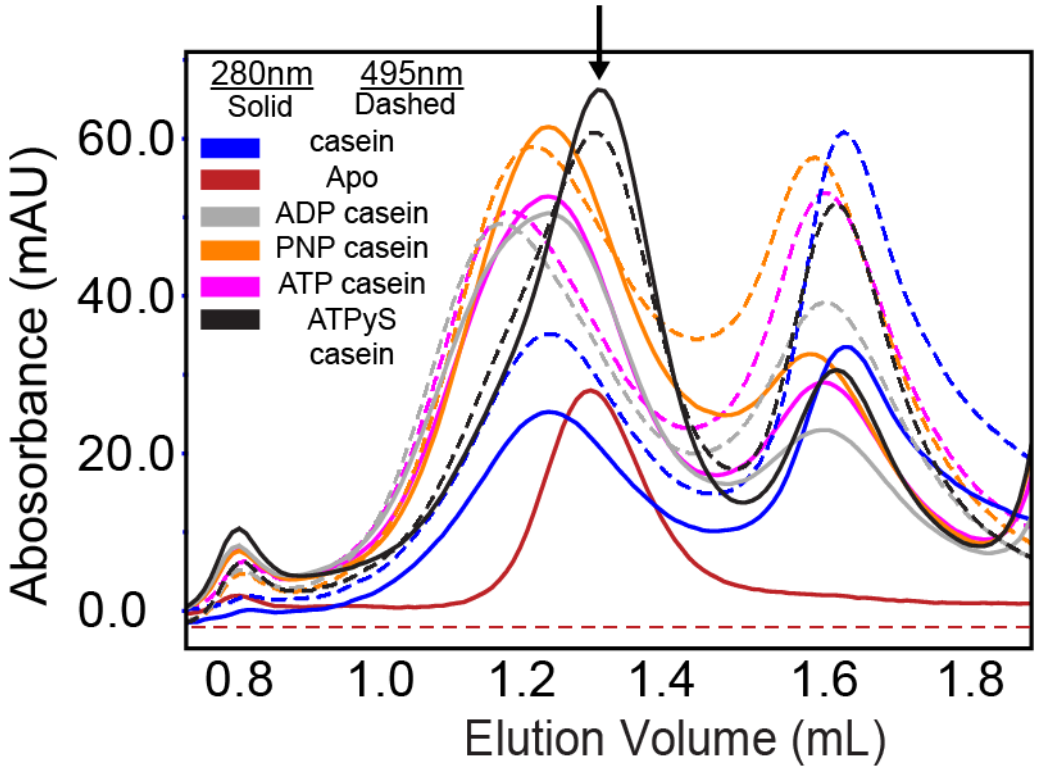

Figure S1. Size exclusion chromatography (SEC) analysis of the Hsp104:casein complex. Hsp104 and casein incubated with the indicated nucleotides, showing a shift in peak elution and alignment of the absorbance curves for protein, 280 (solid), and FITC, 495 (dash) occurs specifically in the presence of ATPγS. Fraction collected for cryo-EM characterization of Hsp104:casein is indicated (arrow).

Supplementry Figure S2

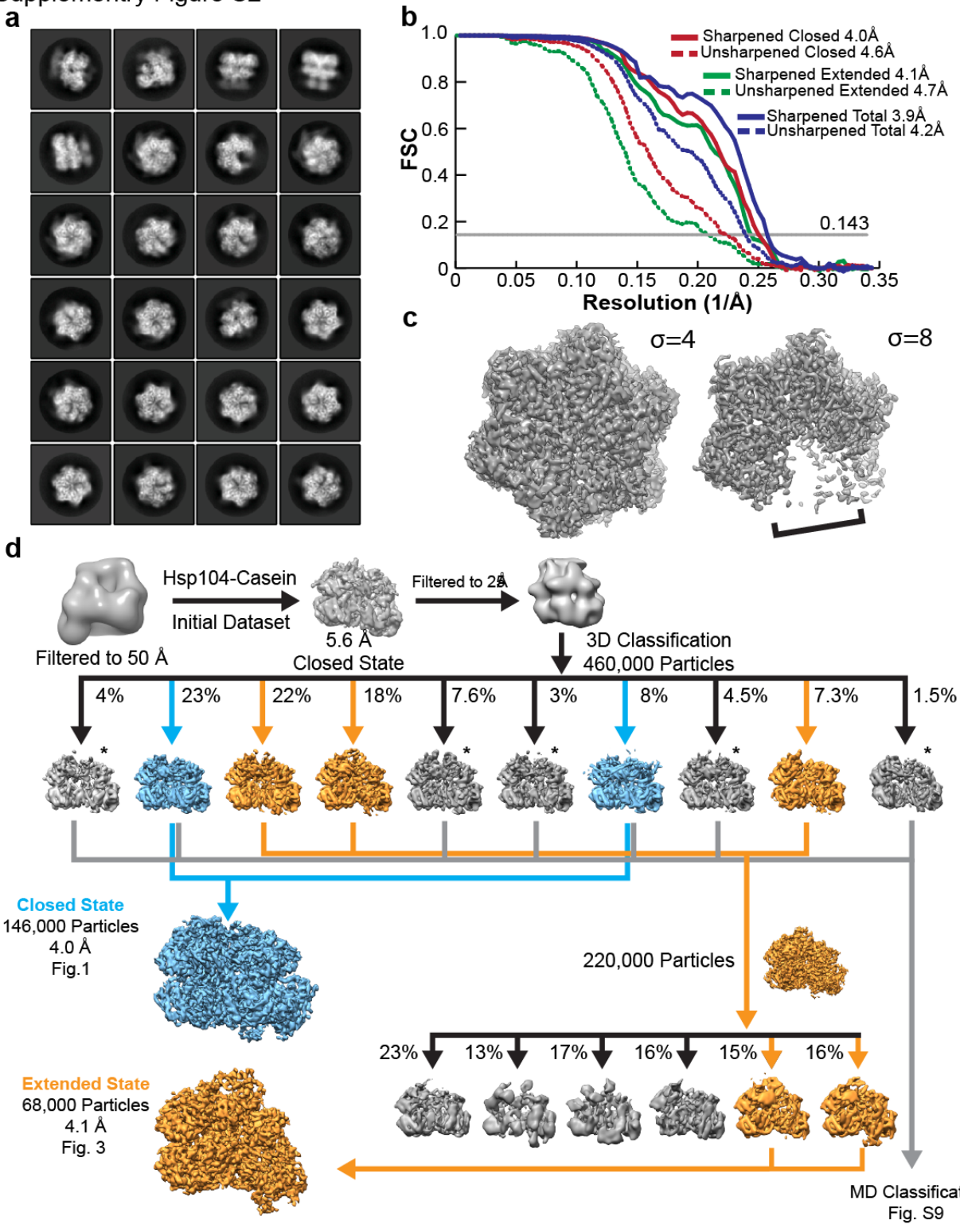

Figure S2. Analysis and cryo-EM processing of the Hsp104:casein complex. (A) Representative reference-free 2D class averages of the purified Hsp104:casein complex incubated with ATPγS. (B) Gold standard FSC curves of the masked and unmasked processed final reconstructions for the total dataset and the closed- and extended-conformation subclasses, determined using Relion *post_processing*(*33*). (C) Top views of the Hsp104:casein 3D reconstruction using the total dataset (following sorting by 2D classification), shown at 4σ and 8σ, showing the loss of density for the lower-resolution mobile two-protomer site (bracket). (D) 3D classification scheme for the Hsp104:casein dataset. Indicated classes were used for closed (blue), extended (orange) and MD class (grey) refinements, with a 3D sub-classification of the extended-state single particles to achieve a better-resolved P6-P1 interface. Classes indicated with an (*) were confirmed to be in the closed state but resulted in no improvements in resolution and thus were excluded during the final refinements.

Supplementry Figure S3

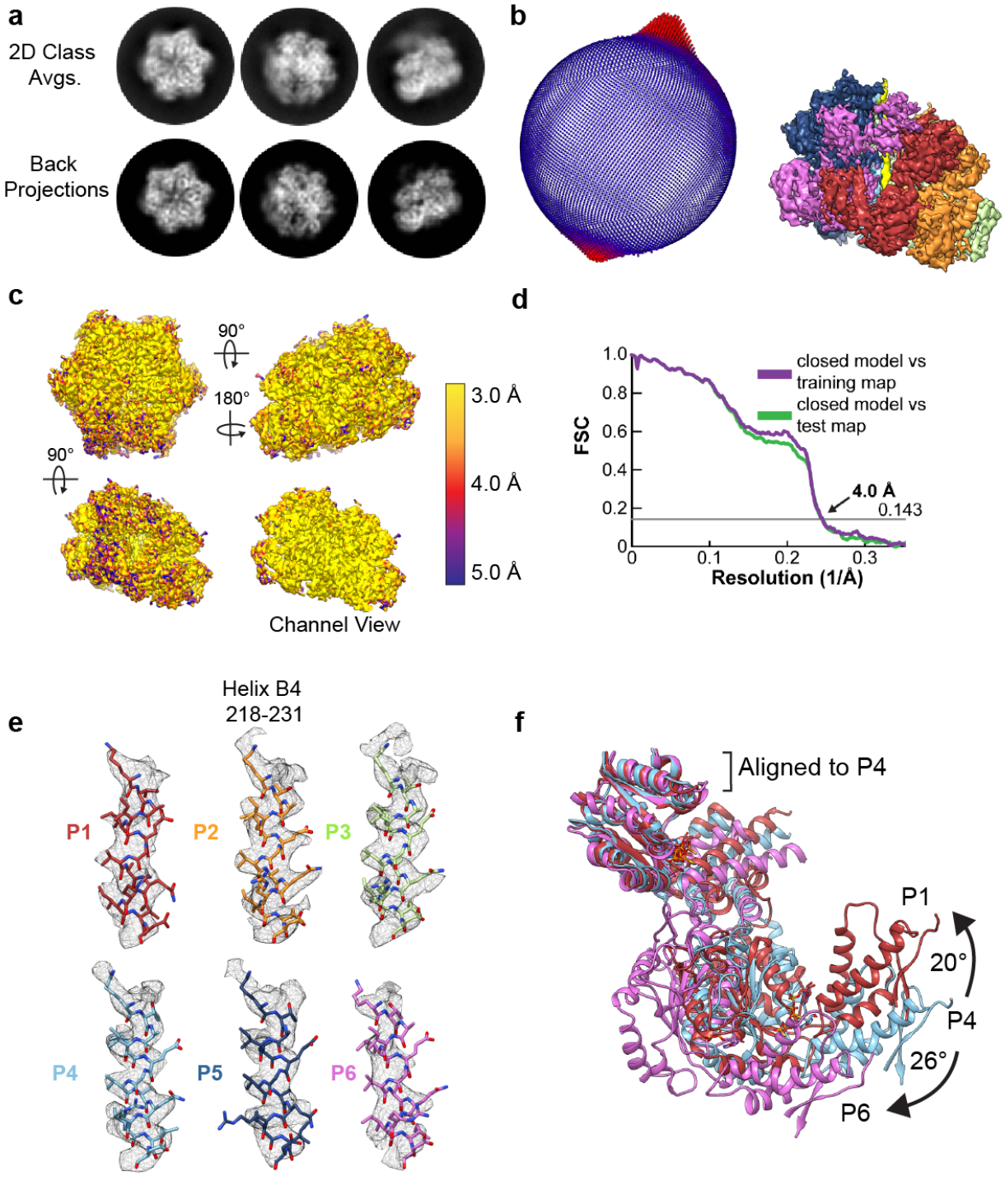

Figure S3. Validation of the Hsp104:casein closed state reconstruction. (A) 2D projections from reference-free classification matched to back projections of the final map. (B) Angular

distribution of particles for the final refinement is shown with the corresponding view of the map. The number of particles for each orientation is indicated by color (blue = low and red = high) and the size of the bar. (C) Resolution shown across the final 3D map for the reconstruction of the closed state, determined using Resmap(*35*). (D) FSC curve of the closed model vs. training map (purple) and test map (green), following molecular model determination in Rosetta (*40*). (E) Helix B4 from each protomer showing cryo-EM density (mesh) and atomic model (sticks). (F) Superposition of the mobile protomers, P1 (red) and P6 (magenta), with a stable protomer, P4 (blue), aligned to the NBD1 large subdomain to show conformational differences.

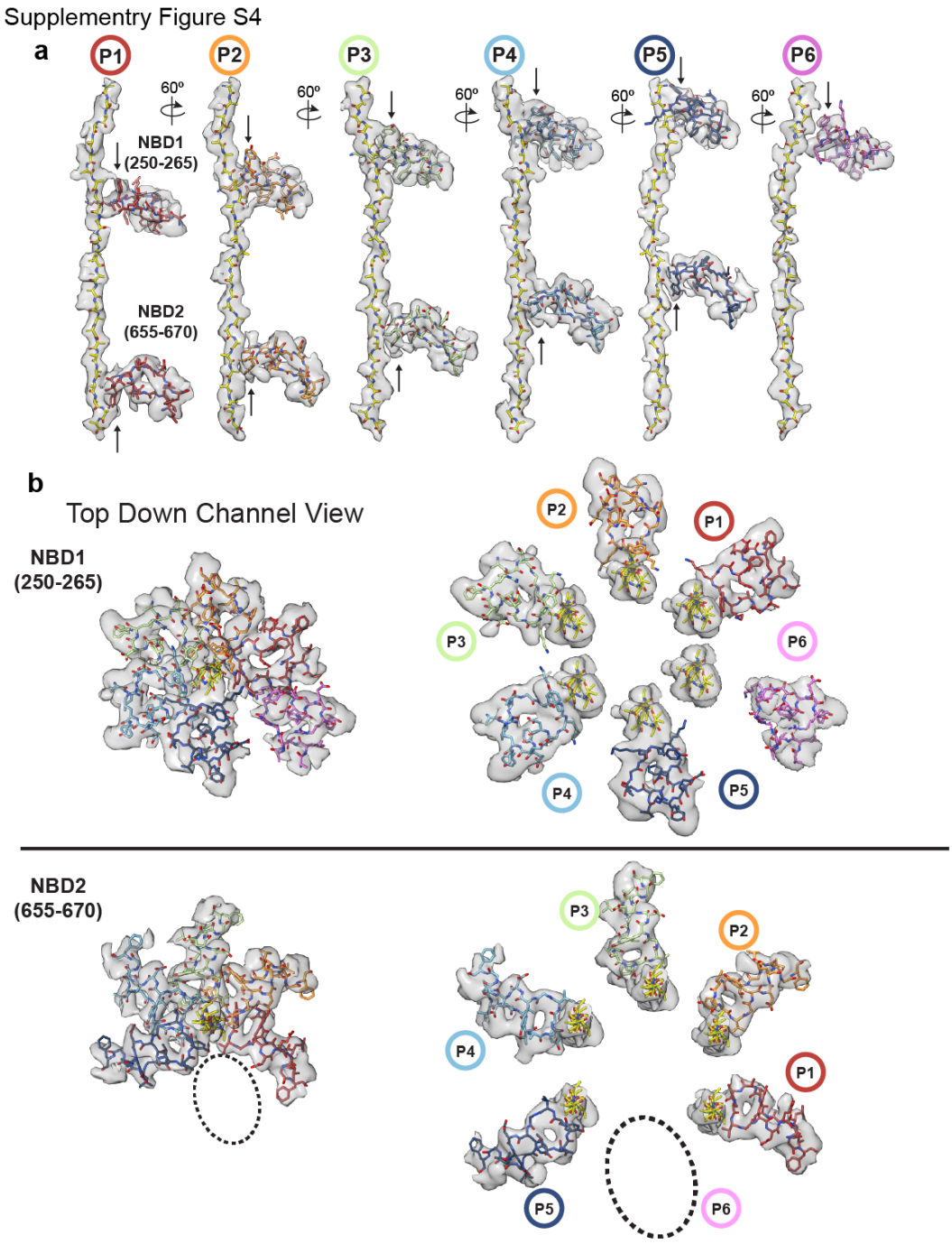

Figure S4. Pore loop-substrate contacts in the Hsp104:casein closed state. (A) Side-view of segmented NBD1 and NBD2 pore loops, including Y257 and Y662 (arrows), shown along the substrate polypeptide (yellow). (B) Top view of the NBD1 and NB2 pore loop-substrate arrangement.

Supplemenatry Figure S5

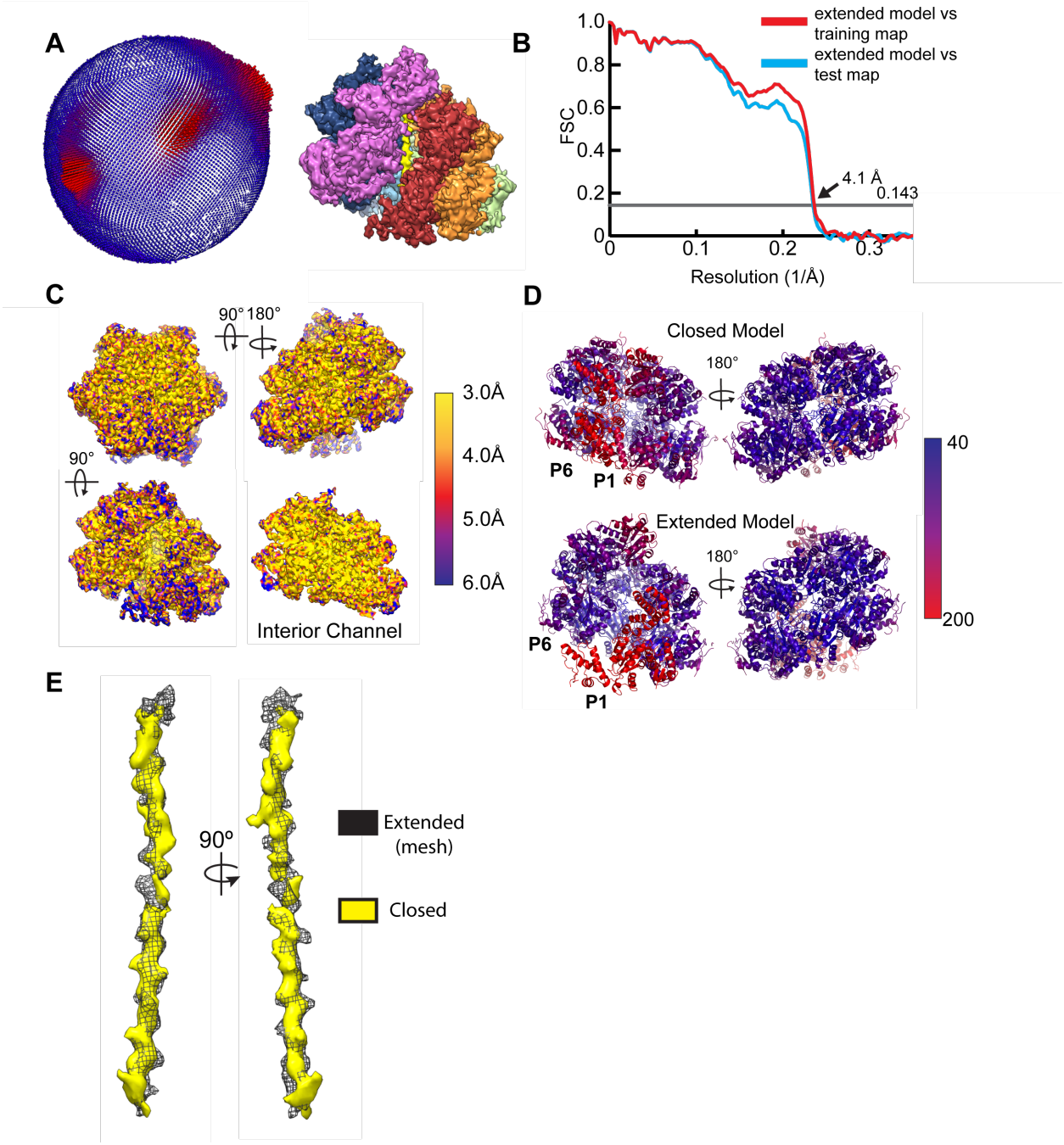

Figure S5. Refinement and analysis of the Hsp104:casein extended state reconstruction. (A) Angular distribution image of particles for the final round of refinement of the extended state, as in Fig. S3b. (B) FSC curve of the final model comparing the training (red) and test (blue) models used during refinement and model building with Rosetta(*40*). (C) Overlay of closed (yellow) and

extended (black mesh) polypeptide density shown following alignment of the AAA+ domains. (D) Resolution across the final map determined by Resmap(*35*) analysis. (E) Closed and extended models colored by the temperature factor, determined with Rosetta, identifying distinct flexibility of the P1 and P6 protomers in the two states (red).

Supplementry Figure S6

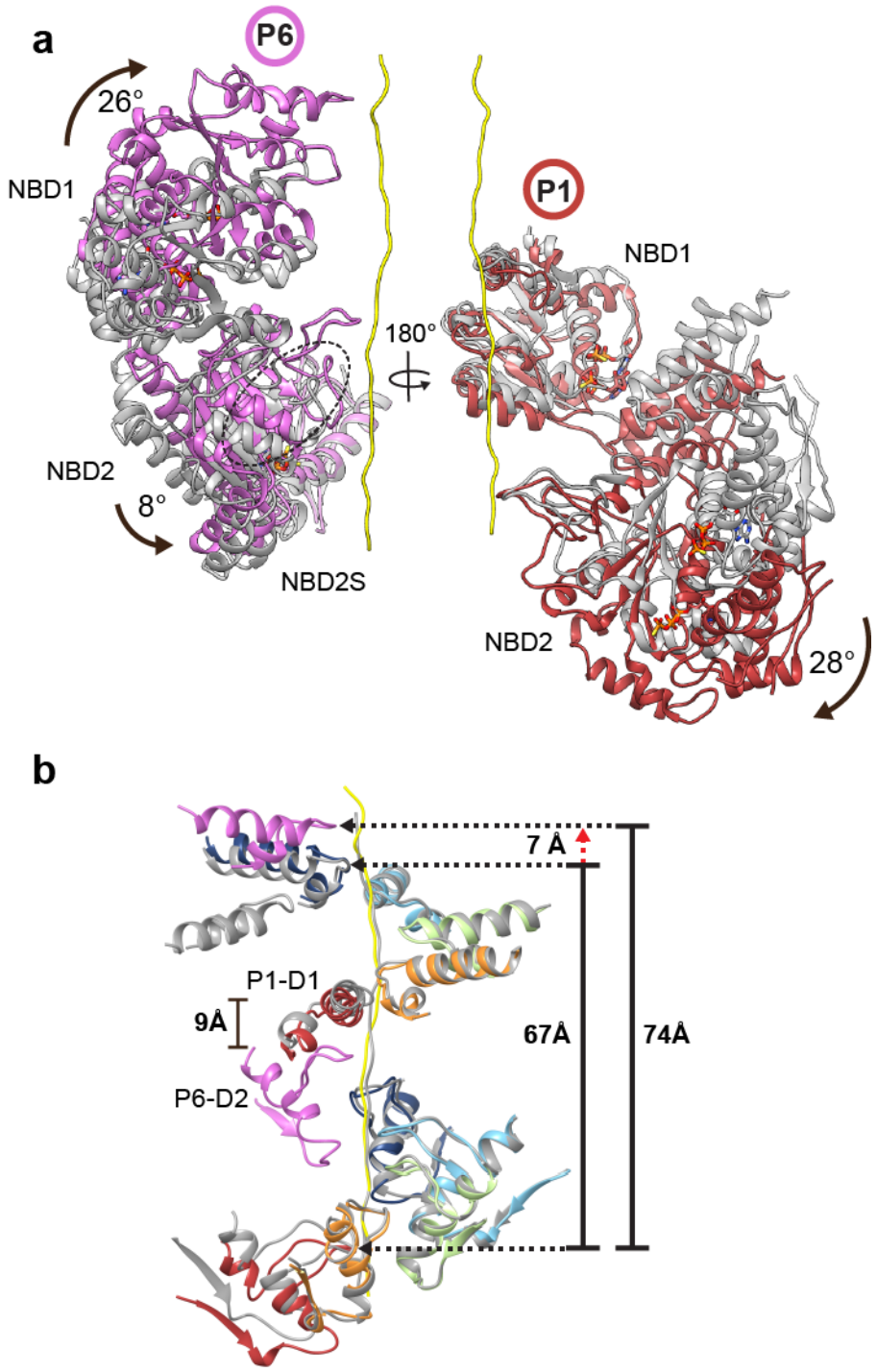

Figure S6. Conformational differences and pore loop-substrate contacts in the closed and extended states. (A) Overlay of the P6 and P1 protomers in the closed (grey) and extended (magenta and red, respectively) states following alignment of the hexamers identifying specific

NBD1 and NBD2 rotations. (B) Overlay of the of the pore loops and polypeptide substrate in the closed (grey) and extended (colored by protomer) states showing complete substrate engagement and a 7 Å translocation step along the polypeptide that occurs in the extended state.

Supplementry Figure S7

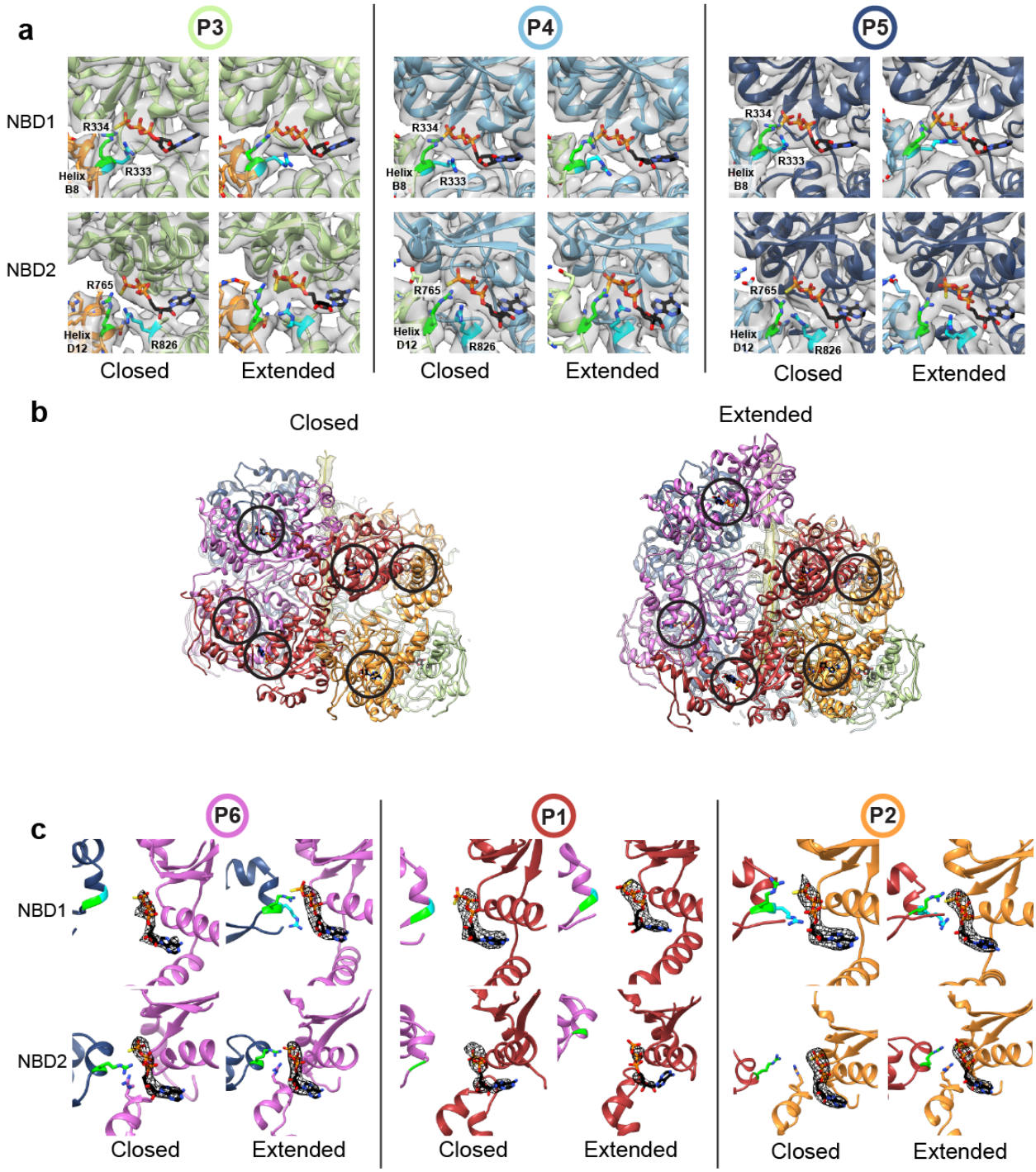

Figure S7. **Arrangement of the nucleotide pockets in the closed and extended states.** (A) Cryo-EM density and model for the NBD1 and NBD2 nucleotide pockets of P3-P5, in the closed and extended states, showing an active configuration. The Arg finger residues (green), R334

(NBD1) and R765 (NBD2), from the adjacent protomer (helix B8 and helix D12, respectively) and the putative NBD1 sensor 2, R333 (cyan) and the NBD2 sensor 2, R826 (cyan) are shown. (B) Hexamer models of the extended and closed states, colored by protomer, showing the mobile protomer face and location of the nucleotide pockets (circles). (C) Nucleotide pockets for protomers P6, P1 and P2 in the closed and extended states with difference maps (displayed as mesh with a threshold of σ = ~7) shown. These were generated by subtracting an apo map (generated from the model) from final reconstruction in order to show nucleotide occupancy.

Supplementry Figure S8

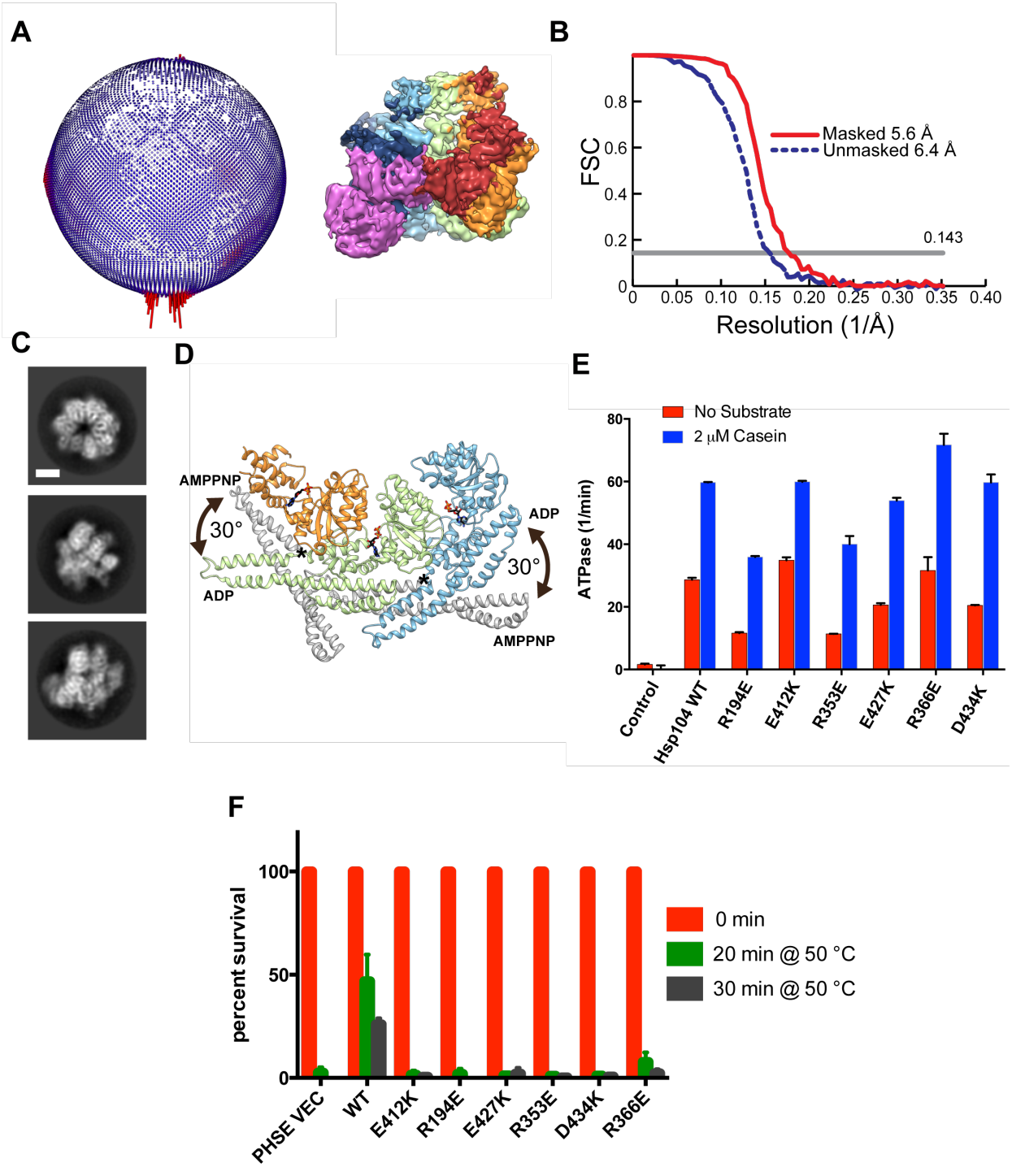

Figure S8. Refinement of the Hsp104-ADP and analysis of putative MD-NBD1 contacts. (A) Angular distribution image of particles for the Hsp104-ADP reconstruction shown as in Fig. S3b. (B) Gold standard(*33*) FSC curve of the final masked and unmasked 3D refinement of Hsp104-

ADP. (C) Reference-free class averages of Hsp104-ADP showing spiral, open conformation (scale bar = 50 Å). (D) Overlay of MD and NBD1 for Hsp104-AMPPNP (grey) and Hsp104-ADP (colored by protomer) reconstructions aligned to their AAA+ domains showing MD conformational changes. (E) ATPase activity of wildtype Hsp104 and L1-NBD1 variants identified in the Hsp104-AMPPNP structure in the absence (red) and presence (blue) of casein (2 μM). Values represent mean±SD (n=2). (F) Δ*hsp104* yeast cells harboring empty pHSEgc vector or the indicated pHSEgc-Hsp104 variant (WT, E412K, R194E, E427K, R535E, D434K, or R366E) were grown to mid-log phase in SD-his. Prior to the 50°C heat treatment, matched cultures were preincubated at 37°C for 30 min. Following treatment at 50°C for 0 min (red bars), 20 min (green bars), or 30 min (black bars) cells were transferred to ice and plated on SD-his. After 2 days at 30°C, survival (%) was quantified. Values represent mean±SD (n=3).

Supplementry Figure S9

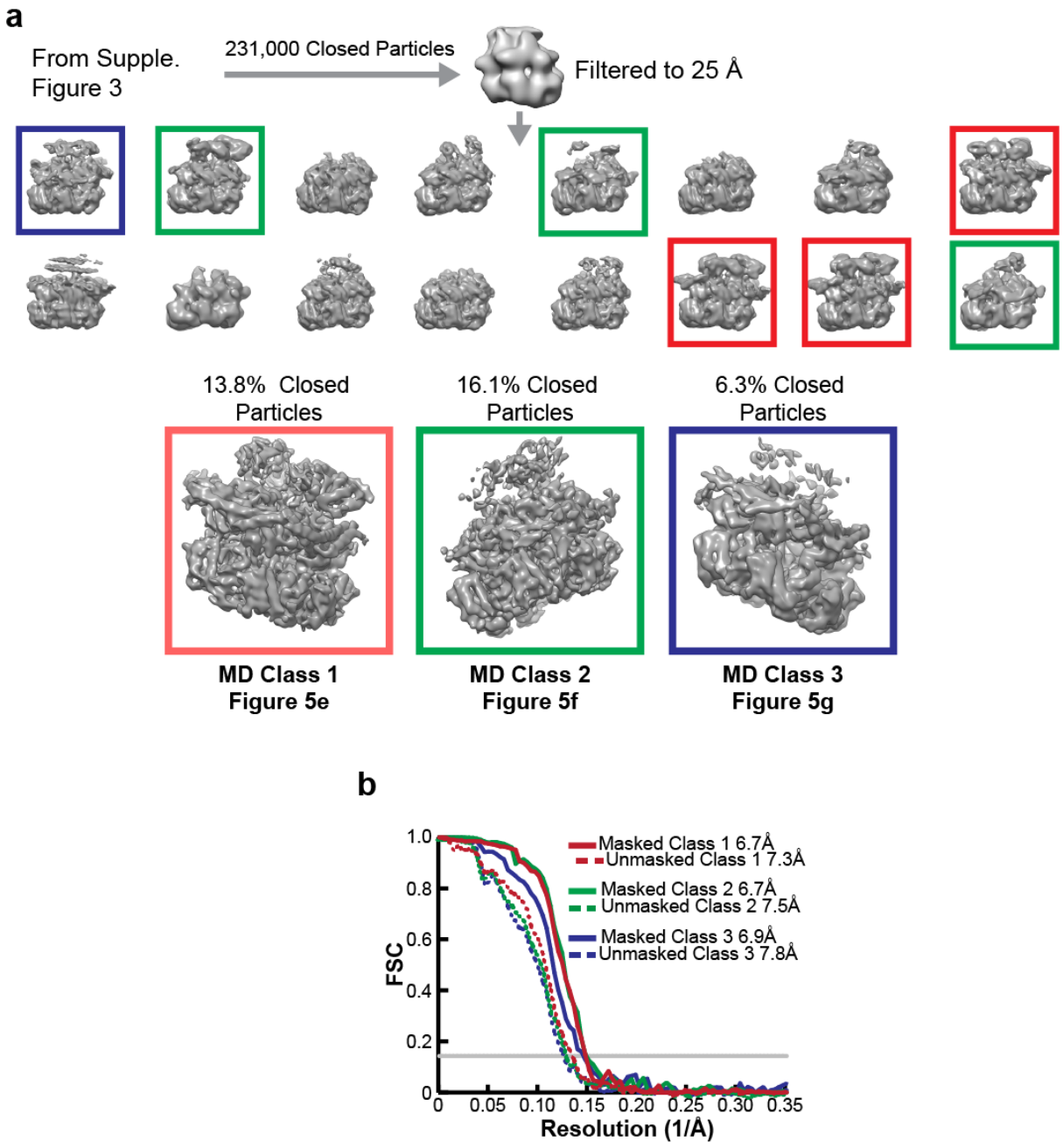

Figure S9. 3D classification scheme and refinement of MD Class1-3. (A) Scheme showing 3D sub-classification of the closed state classes performed following initial classification (Fig. S2D) resulting in MD Class 1 (red) Class 2 (green) and Class 3 (blue) reconstructions that

identify distinct ATP- and ADP-state MD conformations. (B) Gold standard FSC curves of the final masked and unmasked 3D refinements of the indicated MD classes.

Supplementry Figure S10

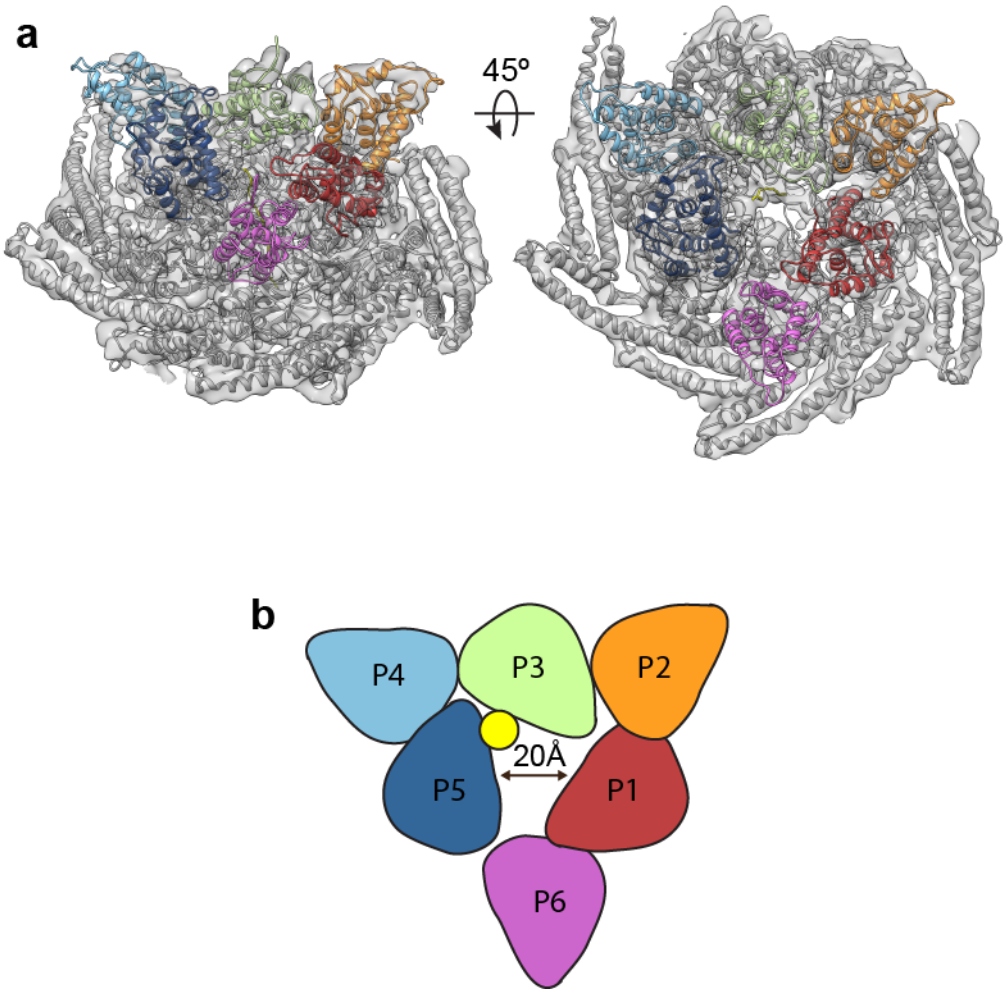

Figure S10. Arrangement of NTDs in MD Class1. (A) Map and model of MD Class 1 showing the NTD-NBD1 region, NTDs colored corresponding to protomer, as above. (B) Schematic based on the model showing alternating orientation of the NTDs and triangular arrangement of the channel entrance with substrate (yellow) positioned off-center, adjacent P3 and P5.

Supplementry Figure S11

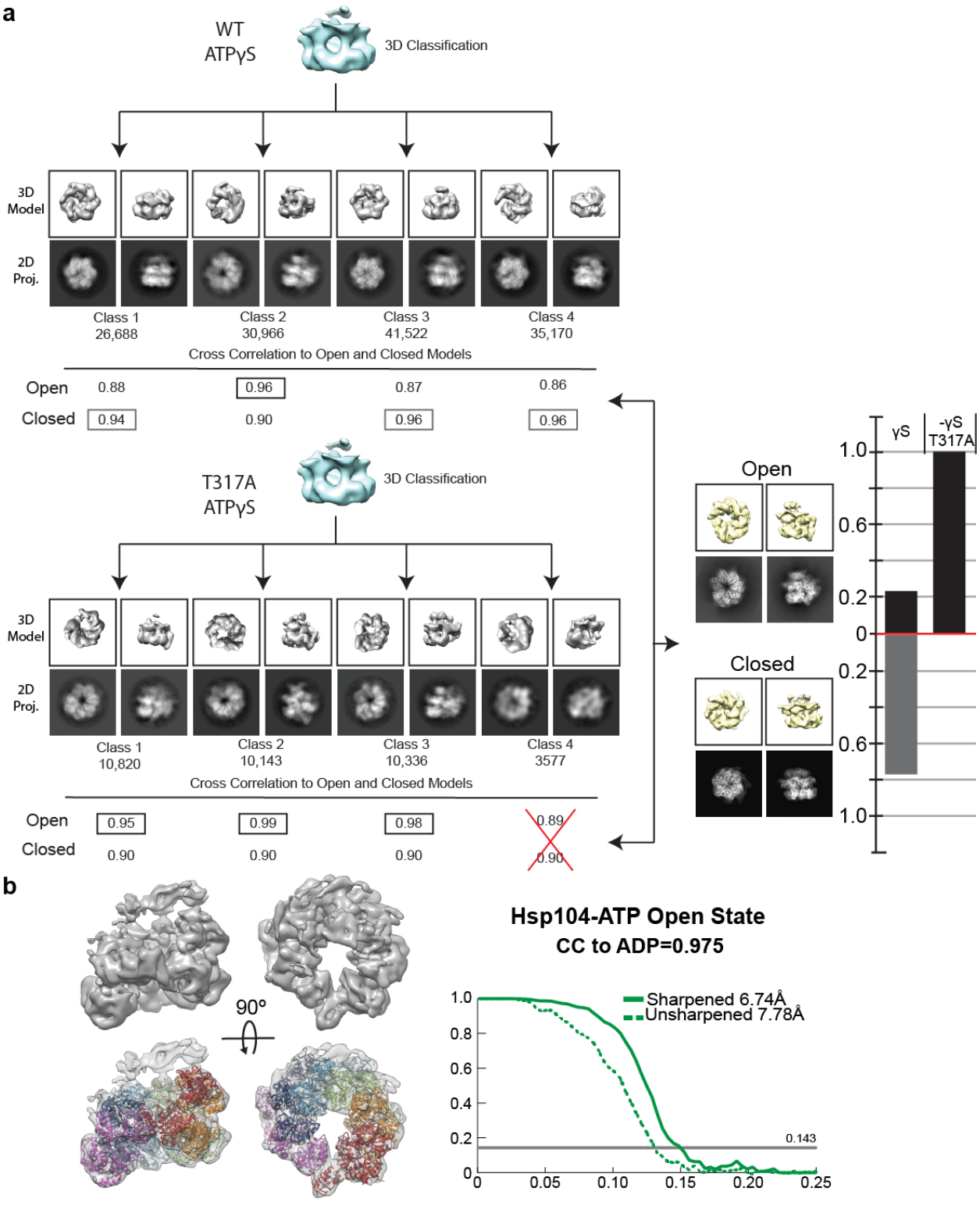

Fig. S11. Classification analysis scheme to identify the fraction of the open and closed states. (A) 3D classification scheme of wildtype and T317A mutant Hsp104 incubated with

ATPγS and cross-correlation analysis to determine the classes that match the open or closed states (cross-correlation ≥ 0.93 indicates a match). Note that the top views of the 2D projections for each class clearly depict the open and closed conformation and agree with the cross-correlation analysis. Classes with cross-correlation values < 0.93 for both the open and closed model comparisons were considered poorly defined and excluded from further analysis (red X). Resulting bar graph is shown of wildtype Hsp104-ATPγS and T317A Hsp104-ATPγS showing the fraction of particles that match the open or closed conformations, determined from the above cross correlation analysis. (B) Reconstruction, model and FSC cure of Hsp104-ADP showing open spiral conformation and high cross correlation to the Hsp104-ADP map (0.975).

Supplementry Figure S12

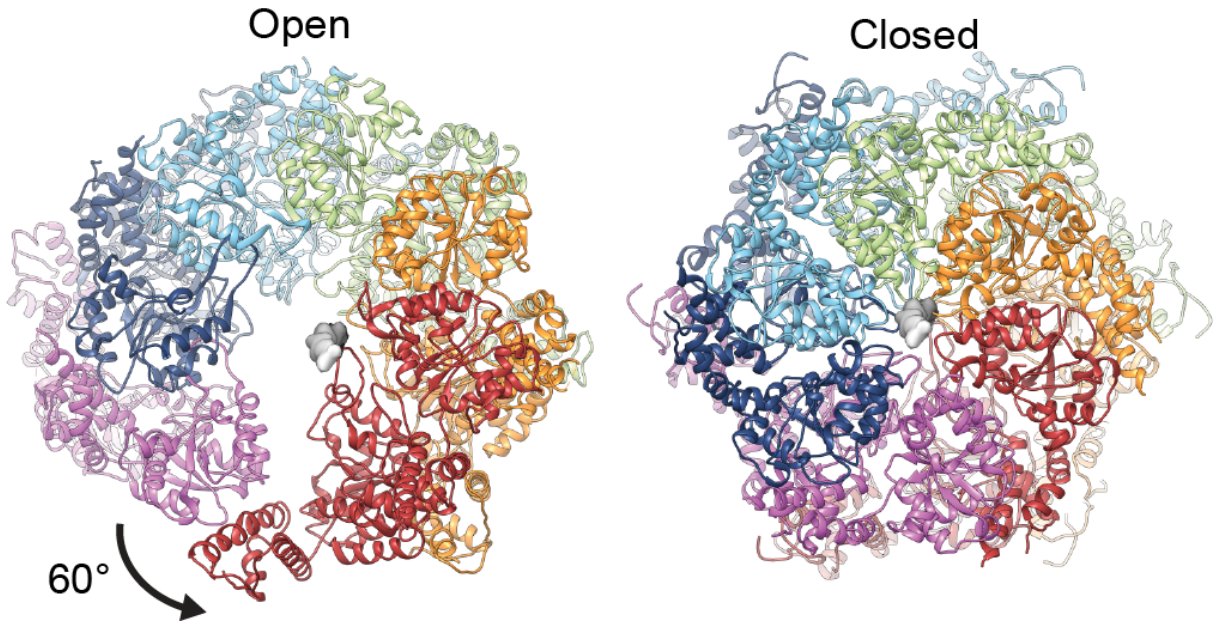

Figure S12. Comparison of the channel in the open and closed state. Top views of open and closed states, colored by protomers, showing the hexamer undergoes a ~60° rotation.

	Total	Closed	Extended	MD Class 1	MD Class 2	MD Class 3	ADP
Data Collection							
Microscope	Titan Krios						
Direct Detector	Gatan K2 Summit						
Voltage	300 kV						
Magnification	50,000x						
Pixel Size	1.00Å						
Dose Rate	4.8 electrons/pixel/sec						
Total Dose	10 per sec						
# of Frames	48 electrons						
Defocus Range	1.5-3.5 µm						
Movies Taken	2764						2422
Data Processing							
Single Particles	454,924	146,463	68,459	31,969	37,361	14,494	124,933
Symmetry	C1	C1	C1	C1	C1	C1	C1
Resolution (Unmasked)	4.19 Å	4.57 Å	4.74 Å	7.31 Å	7.53 Å	7.76 Å	6.40 Å
Resolution (Masked)	3.94 Å	4.00 Å	4.13 Å	6.73 Å	6.73 Å	6.91 Å	5.64 Å
Applied B-Factor	-200	-176	-136	-381	-446	-183	-192
Model Composition							
Residues		3485	3502	4895			3906
Nucleotides		12	12	12			12
Model Scores							
Ramachandran Outliers		0.90%	1.41%	1.75%			1.65%
Ramachandran Favored		95.21%	94.02%	92.51%			92.67%
Molprobity Score		1.81	1.92	1.88			1.84
Clashscore		8.88	9.90	7.53			6.82
Poor Rotamers		0.71%	0.67%	0.14%			0.27%
Favored Rotamers		98.59%	98.39%	98.97%			99.25%
EMBD ID		8697	8746	8745			8744
PBD ID		5VJH	5VYA	5VY9			5VY8

Table S1. Data collection, processing and model parameters for all reconstructions and atomic models.

Dataset		Class 1	Class 2	Class 3	Class 4	Total
AMPPNP	Particles	42562	43654	26405	48405	161026
	Open CC	**0.98**	**0.96**	0.88	0.92	100%
	Closed CC	0.90	0.91	0.90	0.90	0%
ADP	Particles	22101	38645	19539	44649	124934
	Open CC	**0.96**	**0.98**	0.89	**0.99**	100%
	Closed CC	0.91	0.92	0.92	0.87	0%
ATP	Particles	17737	37881	10344	13195	79157
	Open CC	**0.99**	**0.99**	0.85	**0.97**	87%
	Closed CC	0.90	0.89	**0.95**	0.93	13%
ATP Casein	Particles	13966	27109	18803	17627	77505
	Open CC	0.88	**0.97**	**0.95**	**0.98**	82%
	Closed CC	**0.93**	0.89	0.90	0.90	18%
ATPγS	Particles	26688	30966	41522	35170	134346
	Open CC	0.88	**0.96**	0.87	0.86	23%
	Closed CC	**0.94**	0.90	**0.96**	**0.96**	77%
ATPγS Casein	Particles	148006	136162	115782	54986	454936
	Open CC	0.86	0.84	0.85	0.87	0%
	Closed CC	**0.97**	**0.99**	**0.97**	**0.98**	100%
ATP T317A	Particles	5952	9890	8392	7826	32060
	Open CC	**0.96**	**0.99**	0.85	**0.99**	100%
	Closed CC	0.91	0.90	0.87	0.90	0%
ATPγS T317A	Particles	10820	10143	10336	3577	34876
	Open CC	**0.95**	**0.99**	**0.98**	0.89	100%
	Closed CC	0.90	0.90	0.91	0.90	0%
ATP N728A	Particles	11977	19951	7906	16123	55957
	Open CC	**0.94**	0.88	0.91	0.87	21%
	Closed CC	0.89	**0.95**	**0.96**	**0.93**	79%
ATPγS N728A	Particles	10624	5872	9105	21211	46812
	Open CC	**0.98**	0.88	**0.93**	0.86	42%
	Closed CC	0.91	**0.93**	0.91	**0.98**	58%

Table S2. Cross-correlation analysis and particle distributions for the open and closed hexamer states following 3D classification.

Supplementary Movie Legends

Movie S1. Closed-extended ratchet-like conformational change of Hsp104 substrate-bound states. The Hsp104 hexamer closed- and extended-state structures are shown with the protomers (ribbons), colored as in Figure 1E, and the bound polypeptide substrate (yellow, with cryo-EM density). The P4 protomers in the two hexamer structures were aligned and a morph is shown going from the closed to extended states for the complete hexamer and for protomers P1, P2 and P6, identifying conformational changes that result in substrate interactions by P6 and the two-turn spiral arrangement of pore-loops.

Movie S2. Closed-extended rotary model of polypeptide translocation by Hsp104. Morph of the closed to extended conformational change, as in Video 1, applied sequentially around the hexamer counterclockwise from P1 to P6. A 40 amino-acid strand was modeled based on the extended-state structure, revealing processive, two-amino acid steps result translocation of 12 residues during one complete cycle around the hexamer.

Movie S3. MD conformational change between the ATP and ADP states. Morph of MD conformations identified in the Hsp104-AMPPNP(*9*) (ATP state) and Hsp104-ADP structures. The AAA+ domains of the P4 protomers were aligned for the two hexamer structures. The morph identifies a 30° rotation around residue 409 resulting in the distinct MDL1-NBD1 and MDL1-MDL3 interactions in the ATP and ADP states, respectively.

Movie S4. Rearrangement between the open and closed Hsp104 states results in a large, 65 Å translocation step. The movie depicts the conformational change between the open and closed

states along a polypeptide modeled based on the closed state. For the morph, the P1 protomers were aligned within the hexamer models of Hsp104-ADP and Hsp104:casein.

Author Contributions:

S.G and A.Y. designed experiments, performed cryo-EM sample preparation, data collection and analysis, and wrote the manuscript; J.L. and M.E.J. purified Hsp104 variants, designed and performed experiments, and edited the manuscript; A.R. collected and analyzed cryo-EM data; N.K. purified Hsp104 variants, designed and performed experiments, and edited the manuscript; C.B. and E.S. designed and performed experiments, and edited the manuscript; E.C., M.T., and K.M. purified Hsp104 variants and edited the manuscript; M.S. supervised cryo-EM data collection; J.S. designed experiments and edited the manuscript; D.S. designed and supervised the study and edited the manuscript.

References and Notes

1. A. O. Olivares, T. A. Baker, R. T. Sauer, Mechanistic insights into bacterial AAA+ proteases and protein-remodelling machines. *Nat. Rev. Microbiol.* **14**, 33–44 (2016). doi:10.1038/nrmicro.2015.4 Medline

2. E. A. Sweeny, J. Shorter, Mechanistic and structural insights into the prion-disaggregase activity of Hsp104. *J. Mol. Biol.* **428**, 1870–1885 (2016). doi:10.1016/j.jmb.2015.11.016 Medline

3. J. P. Erzberger, J. M. Berger, Evolutionary relationships and structural mechanisms of AAA+ proteins. *Annu. Rev. Biophys. Biomol. Struct.* **35**, 93–114 (2006). doi:10.1146/annurev.biophys.35.040405.101933 Medline

4. M. E. Jackrel, M. E. DeSantis, B. A. Martinez, L. M. Castellano, R. M. Stewart, K. A. Caldwell, G. A. Caldwell, J. Shorter, Potentiated Hsp104 variants antagonize diverse proteotoxic misfolding events. *Cell* **156**, 170–182 (2014). doi:10.1016/j.cell.2013.11.047 Medline

5. Y. Oguchi, E. Kummer, F. Seyffer, M. Berynskyy, B. Anstett, R. Zahn, R. C. Wade, A. Mogk, B. Bukau, A tightly regulated molecular toggle controls AAA+ disaggregase. *Nat. Struct. Mol. Biol.* **19**, 1338–1346 (2012). doi:10.1038/nsmb.2441 Medline

6. J. Lee, J.-H. Kim, A. B. Biter, B. Sielaff, S. Lee, F. T. F. Tsai, Heat shock protein (Hsp) 70 is an activator of the Hsp104 motor. *Proc. Natl. Acad. Sci. U.S.A.* **110**, 8513–8518 (2013). doi:10.1073/pnas.1217988110 Medline

7. R. Lum, J. M. Tkach, E. Vierling, J. R. Glover, Evidence for an unfolding/threading mechanism for protein disaggregation by *Saccharomyces cerevisiae* Hsp104. *J. Biol. Chem.* **279**, 29139–29146 (2004). doi:10.1074/jbc.M403777200 Medline

8. P. Tessarz, A. Mogk, B. Bukau, Substrate threading through the central pore of the Hsp104 chaperone as a common mechanism for protein disaggregation and prion propagation. *Mol. Microbiol.* **68**, 87–97 (2008). doi:10.1111/j.1365-2958.2008.06135.x Medline

9. A. L. Yokom, S. N. Gates, M. E. Jackrel, K. L. Mack, M. Su, J. Shorter, D. R. Southworth, Spiral architecture of the Hsp104 disaggregase reveals the basis for polypeptide translocation. *Nat. Struct. Mol. Biol.* **23**, 830–837 (2016). doi:10.1038/nsmb.3277 Medline

10. S. M. Doyle, J. Shorter, M. Zolkiewski, J. R. Hoskins, S. Lindquist, S. Wickner, Asymmetric deceleration of ClpB or Hsp104 ATPase activity unleashes protein-remodeling activity. *Nat. Struct. Mol. Biol.* **14**, 114–122 (2007). doi:10.1038/nsmb1198 Medline

11. S. Lee, M. E. Sowa, Y. H. Watanabe, P. B. Sigler, W. Chiu, M. Yoshida, F. T. F. Tsai, The structure of ClpB: A molecular chaperone that rescues proteins from an aggregated state. *Cell* **115**, 229–240 (2003). doi:10.1016/S0092-8674(03)00807-9 Medline

12. M. Carroni, E. Kummer, Y. Oguchi, P. Wendler, D. K. Clare, I. Sinning, J. Kopp, A. Mogk, B. Bukau, H. R. Saibil, Head-to-tail interactions of the coiled-coil domains regulate ClpB activity and cooperation with Hsp70 in protein disaggregation. *eLife* **3**, e02481 (2014). doi:10.7554/eLife.02481 Medline

13. P. Wendler, J. Shorter, C. Plisson, A. G. Cashikar, S. Lindquist, H. R. Saibil, Atypical AAA+ subunit packing creates an expanded cavity for disaggregation by the protein-remodeling factor Hsp104. *Cell* **131**, 1366–1377 (2007). doi:10.1016/j.cell.2007.10.047 Medline

14. E. J. Enemark, L. Joshua-Tor, Mechanism of DNA translocation in a replicative hexameric helicase. *Nature* **442**, 270–275 (2006). doi:10.1038/nature04943 Medline

15. F. Abid Ali, L. Renault, J. Gannon, H. L. Gahlon, A. Kotecha, J. C. Zhou, D. Rueda, A. Costa, Cryo-EM structures of the eukaryotic replicative helicase bound to a translocation substrate. *Nat. Commun.* **7**, 10708 (2016). doi:10.1038/ncomms10708 Medline

16. N. D. Thomsen, J. M. Berger, Running in reverse: The structural basis for translocation polarity in hexameric helicases. *Cell* **139**, 523–534 (2009). doi:10.1016/j.cell.2009.08.043 Medline

17. A. Heuck, S. Schitter-Sollner, M. J. Suskiewicz, R. Kurzbauer, J. Kley, A. Schleiffer, P. Rombaut, F. Herzog, T. Clausen, Structural basis for the disaggregase activity and regulation of Hsp104. *eLife* **5**, e21516 (2016). doi:10.7554/eLife.21516 Medline

18. D. A. Hattendorf, S. L. Lindquist, Cooperative kinetics of both Hsp104 ATPase domains and interdomain communication revealed by AAA sensor-1 mutants. *EMBO J.* **21**, 12–21 (2002). doi:10.1093/emboj/21.1.12 Medline

19. A. Y. Lyubimov, A. Costa, F. Bleichert, M. R. Botchan, J. M. Berger, ATP-dependent conformational dynamics underlie the functional asymmetry of the replicative helicase from a minimalist eukaryote. *Proc. Natl. Acad. Sci. U.S.A.* **109**, 11999–12004 (2012). doi:10.1073/pnas.1209406109 Medline

20. E. Skordalakes, J. M. Berger, Structure of the Rho transcription terminator: Mechanism of mRNA recognition and helicase loading. *Cell* **114**, 135–146 (2003). doi:10.1016/S0092-8674(03)00512-9 Medline

21. P. Śledź, P. Unverdorben, F. Beck, G. Pfeifer, A. Schweitzer, F. Förster, W. Baumeister, Structure of the 26S proteasome with ATP-γS bound provides insights into the mechanism of nucleotide-dependent substrate translocation. *Proc. Natl. Acad. Sci. U.S.A.* **110**, 7264–7269 (2013). doi:10.1073/pnas.1305782110 Medline

22. M. Zhao, S. Wu, Q. Zhou, S. Vivona, D. J. Cipriano, Y. Cheng, A. T. Brunger, Mechanistic insights into the recycling machine of the SNARE complex. *Nature* **518**, 61–67 (2015). doi:10.1038/nature14148 Medline

23. M. E. DeSantis, E. H. Leung, E. A. Sweeny, M. E. Jackrel, M. Cushman-Nick, A. Neuhaus-Follini, S. Vashist, M. A. Sochor, M. N. Knight, J. Shorter, Operational plasticity enables Hsp104 to disaggregate diverse amyloid and nonamyloid clients. *Cell* **151**, 778–793 (2012). doi:10.1016/j.cell.2012.09.038 Medline

24. T. Li, C. L. Weaver, J. Lin, E. C. Duran, J. M. Miller, A. L. Lucius, *Escherichia coli* ClpB is a non-processive polypeptide translocase. *Biochem. J.* **470**, 39–52 (2015). doi:10.1042/BJ20141457 Medline

25. M. Wehmer, E. Sakata, Recent advances in the structural biology of the 26S proteasome. *Int. J. Biochem. Cell Biol.* **79**, 437–442 (2016). doi:10.1016/j.biocel.2016.08.008 Medline

26. S. E. Glynn, A. Martin, A. R. Nager, T. A. Baker, R. T. Sauer, Structures of asymmetric ClpX hexamers reveal nucleotide-dependent motions in a AAA+ protein-unfolding machine. *Cell* **139**, 744–756 (2009). doi:10.1016/j.cell.2009.09.034 Medline

27. M. E. Matyskiela, G. C. Lander, A. Martin, Conformational switching of the 26S proteasome enables substrate degradation. *Nat. Struct. Mol. Biol.* **20**, 781–788 (2013). doi:10.1038/nsmb.2616 Medline

28. M. P. Torrente, L. M. Castellano, J. Shorter, Suramin inhibits Hsp104 ATPase and disaggregase activity. *PLOS ONE* **9**, e110115 (2014). doi:10.1371/journal.pone.0110115 Medline

29. E. M. Redwan, B. Xue, H. A. Almehdar, V. N. Uversky, Disorder in milk proteins: Caseins, intrinsically disordered colloids. *Curr. Protein Pept. Sci.* **16**, 228–242 (2015). doi:10.2174/1389203716666150224145900 Medline

30. X. Li, S. Zheng, D. A. Agard, Y. Cheng, Asynchronous data acquisition and on-the-fly analysis of dose fractionated cryoEM images by UCSFImage. *J. Struct. Biol.* **192**, 174–178 (2015). doi:10.1016/j.jsb.2015.09.003 Medline

31. T. Grant, N. Grigorieff, Measuring the optimal exposure for single particle cryo-EM using a 2.6 Å reconstruction of rotavirus VP6. *eLife* **4**, e06980 (2015). doi:10.7554/eLife.06980 Medline

32. A. Rohou, N. Grigorieff, CTFFIND4: Fast and accurate defocus estimation from electron micrographs. *J. Struct. Biol.* **192**, 216–221 (2015). doi:10.1016/j.jsb.2015.08.008 Medline

33. S. H. Scheres, RELION: Implementation of a Bayesian approach to cryo-EM structure determination. *J. Struct. Biol.* **180**, 519–530 (2012). doi:10.1016/j.jsb.2012.09.006 Medline

34. G. C. Lander, S. M. Stagg, N. R. Voss, A. Cheng, D. Fellmann, J. Pulokas, C. Yoshioka, C. Irving, A. Mulder, P.-W. Lau, D. Lyumkis, C. S. Potter, B. Carragher, Appion: An integrated, database-driven pipeline to facilitate EM image processing. *J. Struct. Biol.* **166**, 95–102 (2009). doi:10.1016/j.jsb.2009.01.002 Medline

35. A. Kucukelbir, F. J. Sigworth, H. D. Tagare, Quantifying the local resolution of cryo-EM density maps. *Nat. Methods* **11**, 63–65 (2014). doi:10.1038/nmeth.2727 Medline

36. M. Biasini, S. Bienert, A. Waterhouse, K. Arnold, G. Studer, T. Schmidt, F. Kiefer, T. Gallo Cassarino, M. Bertoni, L. Bordoli, T. Schwede, SWISS-MODEL: Modelling protein tertiary and quaternary structure using evolutionary information. *Nucleic Acids Res.* **42**, W252–W258 (2014). doi:10.1093/nar/gku340 Medline

37. P. Emsley, B. Lohkamp, W. G. Scott, K. Cowtan, Features and development of Coot. *Acta Crystallogr. D Biol. Crystallogr.* **66**, 486–501 (2010). doi:10.1107/S0907444910007493 Medline

38. P. V. Afonine, R. W. Grosse-Kunstleve, N. Echols, J. J. Headd, N. W. Moriarty, M. Mustyakimov, T. C. Terwilliger, A. Urzhumtsev, P. H. Zwart, P. D. Adams, Towards automated crystallographic structure refinement with phenix.refine. *Acta Crystallogr. D Biol. Crystallogr.* **68**, 352–367 (2012). doi:10.1107/S0907444912001308 Medline

39. F. DiMaio, Y. Song, X. Li, M. J. Brunner, C. Xu, V. Conticello, E. Egelman, T. C. Marlovits, Y. Cheng, D. Baker, Atomic-accuracy models from 4.5-Å cryo-electron microscopy data with density-guided iterative local refinement. *Nat. Methods* **12**, 361–365 (2015). doi:10.1038/nmeth.3286 Medline

40. Y. Song, F. DiMaio, R. Y.-R. Wang, D. Kim, C. Miles, T. Brunette, J. Thompson, D. Baker, High-resolution comparative modeling with RosettaCM. *Structure* **21**, 1735–1742 (2013). doi:10.1016/j.str.2013.08.005 Medline

41. A. B. Biter, S. Lee, N. Sung, F. T. Tsai, Structural basis for intersubunit signaling in a protein disaggregating machine. *Proc. Natl. Acad. Sci. U.S.A.* **109**, 12515–12520 (2012). doi:10.1073/pnas.1207040109 Medline

42. E. A. Sweeny, M. E. Jackrel, M. S. Go, M. A. Sochor, B. M. Razzo, M. E. DeSantis, K. Gupta, J. Shorter, The Hsp104 N-terminal domain enables disaggregase plasticity and potentiation. *Mol. Cell* **57**, 836–849 (2015). doi:10.1016/j.molcel.2014.12.021 Medline

43. E. F. Pettersen, T. D. Goddard, C. C. Huang, G. S. Couch, D. M. Greenblatt, E. C. Meng, T. E. Ferrin, UCSF Chimera—a visualization system for exploratory research and analysis. *J. Comput. Chem.* **25**, 1605–1612 (2004). doi:10.1002/jcc.20084 Medline